Elasticity and Mechanical Behaviour of Granular Materials: Some Insights from Numerical Studies of Simple Systems

Jean-Noël Roux, Mohamed Hassan Khalili, Francesco Froiio, and Chloé Dequeker

Abstract We briefly review the elastic properties of granular materials, as explored in numerical studies of simple model materials by the "discrete element method" (DEM). Elastic or quasielastic responses are obtained as stable contact networks are probed with negligible friction effects. Elastic moduli, at the macroscopic scale, or contact stiffnesses at the contact network scale, have very limited influence on macroscopic constitutive laws ruling quasistatic deformation and inertial flow. The elastic moduli nevertheless provide useful indirect information on internal variables such as coordination and fabric. Singularities in the tensor of elastic moduli are related to the proximity of failure in the microscopic sense (contact network) but not in the macroscopic sense (yield condition). Elastic properties are also useful in the characterization of the directional dependence of incremental stress-strain response, a key ingredient in the identification of instabilities causing localization phenomena.

Keywords Granular materials · Elasticity · Elastoplasticity · Numerical simulation

1 Introduction

Elasticity is often dealt with as an essential ingredient in mechanical models of granular materials [1]. Micromechanical approaches classically involve contact elasticity, combined with friction and viscous dissipation [2]. Macroscopic constitutive laws for granular soils are often assumed in elastoplastic form [3–5], even though the identification of the parameters of such laws might be delicate and the truly elastic range of material behaviour is restricted to very small strains [6].

J.-N. Roux (✉) · M. H. Khalili
Université Paris EST, Laboratoire Navier, Marne-la-Vallée, France
e-mail: jean-noel.roux@ifsttar.fr

F. Froiio · C. Dequeker
Laboratoire de Tribologie et Dynamique des Systèmes, École Centrale de Lyon, Écully, France

P. Giovine et al. (eds.), *Views on Microstructures in Granular Materials*, Advances in Mechanics and Mathematics 44, https://doi.org/10.1007/978-3-030-49267-0_9

Measurements of elastic moduli associated with a linear response to small load or strain increments about well-equilibrated states of grain packs, under controlled confining stress, have quite often been reported in the geomechanics or physics literature, as obtained via static stress-strain relations [7–11], or dynamical means: resonance modes [12–14], or sound propagation [7, 9–11, 14–18]. Those moduli, as probed for typical strain increments of order 10^{-5} or 10^{-6}, differ from the "elastic" ingredients of constitutive laws [4, 6], which are used in practice for considerably larger strains (say, of order 10^{-3} or 10^{-2}).

Numerical simulation studies of model materials, using the "discrete element method" (or DEM), like many experimental studies or modelling attempts, very often investigate either the elastic moduli of equilibrated grain packs under prescribed stresses [19, 20] or the solid material quasistatic rheology [21], thus considering both strain domains separately. Furthermore, numerical studies of elastic properties often focussed on isotropic states, and their sensitivity to the proximity of a "jamming" threshold (transition to a solid-like material resisting shear stress) [22–25], with considerably fewer investigations of anisotropic configurations [26–28]. And, on the other hand, although quite a few DEM studies have successfully explored the moderate to large strain regime associated with particle rearrangements [29–31] with the "Contact Dynamics" method [32, 33], in which grains are dealt with as perfectly rigid and contacts are devoid of elasticity, the theoretical approach known as Granular Solid Hydrodynamics [34, 35] (evoked in [1]) attributes a basic role to an elastic instability in the macroscopic material yield.

It seems thus necessary to better explore and clarify the role of the elastic ingredients of a granular model, and the connections between elastic moduli and constitutive laws or internal material states.

The present paper proposes a contribution to these issues, based on an overview of DEM studies [28, 36–42] of assemblies of spherical beads, with elasticity and friction in their contacts, but devoid of cohesion. The model material and computation methods are described in Sect. 2. The material is subjected to different kinds of loads, and the resulting characteristic behaviours are briefly reviewed in Sect. 3. We then turn to the connections between elastic properties and material state and mechanical properties, first for isotropic and oedometric loading, in which the stresses essentially vary in intensity, in Sect. 4; then for triaxial compression, in which the direction of stresses and the internal state evolve towards failure and plastic flow (Sect. 5). Sect. 6 is a report on some preliminary results in the modelling of non-elastic strains. Some concluding remarks are given in the final part of the chapter, Sect. 7.

2 Model Material and Simulation Procedures

2.1 System and Contact Laws

Spherical beads of diameter a interact via elasticity and friction, with friction coefficient $\mu = 0.3$, supplemented by viscous dissipation in their contacts. Contact elasticity, as in Ref. [36], is modelled with a simplified version of the Hertz-Mindlin law [43]. Specifically, the normal force F_{ij}^N in the contact between beads i and j, the centres of which are located at $\mathbf{r}_i$ and $\mathbf{r}_j$, depends on contact deflection $h_{ij} = a - ||\mathbf{r}_j - \mathbf{r}_i||$, as

$$F_{ij}^N = \frac{\tilde{E}\sqrt{a}}{3} h_{ij}^{3/2}, \tag{1}$$

in which notation $\tilde{E} = E/(1-\nu^2)$ is introduced, combining the Young modulus E and the Poisson ratio ν of the solid material within the beads. Equation (1) entails that the normal stiffness expressing the response to small variations of deflection $|h_{ij}|$ in the contact varies as

$$K_{ij}^N = \frac{\tilde{E}\sqrt{a}}{2} |h_{ij}|^{1/2} = \frac{3^{1/3}}{2} \tilde{E}^{2/3} a^{1/3} \left(F_{ij}^N\right)^{1/3}. \tag{2}$$

The tangential elastic force $\mathbf{F}_{ij}^T$ [36, 42] is incrementally related to the relative tangential displacement $\delta\mathbf{u}_{ij}^T$ in the contact, by the stiffness coefficient K^T, assumed proportional to K^N:

$$d\mathbf{F}_{ij}^T = K_{ij}^T \, d\left(\delta\mathbf{u}_{ij}^T\right), \text{ with } K_{ij}^T = \frac{2-2\nu}{2-\nu} K_{ij}^N. \tag{3}$$

Tangential stiffness K^T should be suitably rescaled whenever the normal elastic force decreases, in order to avoid spurious elastic energy creation [36, 44].

The Coulomb condition enforces inequality $||\mathbf{F}_{ij}^T|| \leq \mu F_{ij}^N$. As explained in [36, 45], contact forces also have to follow the general motion of the grain pair (maintaining the objectivity of the model).

While all simulations use the elastic properties of glass, $E = 70\,\text{GPa}$ and $\nu = 0.3$, results, if expressed in dimensionless form, exactly apply to all materials sharing the same dimensionless characteristics μ and ν. A normal viscous force is added to the elastic-frictional one [36, 46], corresponding to a very low coefficient of restitution in binary collisions. This viscous ingredient of contact interaction laws is irrelevant in the simulation of quasistatic processes [2]. Most simulations are carried out in samples of 4000 grains and results are averaged over several realizations. Occasional tests with larger samples revealed no significant size effects.

2.2 Loading Procedures

We consider cuboidal simulation cells and apply periodic boundary conditions in all three directions, following the procedure of Refs. [36, 41, 47]. Cell dimensions L_1, L_2, L_3, parallel to the three axes of coordinates (to which correspond basis unit vectors $\mathbf{e}_1$, $\mathbf{e}_2$, $\mathbf{e}_3$), may vary with prescribed strain rate, or gradually adjust to ensure equilibrium under prescribed stresses. Denoting as σ_1, σ_2, σ_3, the diagonal stresses conjugate to strain components ε_α, $1 \leq \alpha \leq 3$, associated with changes in dimensions L_α, we show results corresponding to isotropic compression ($\sigma_1 = \sigma_2 = \sigma_3 = P$), to oedometric compression (in which σ_1 and ε_1 increase while L_2, L_3 are maintained fixed—$\varepsilon_2 = \varepsilon_3 = 0$), and triaxial compression (increase of σ_1 and ε_1, while $\sigma_2 = \sigma_3$ are kept constant).

In both strain rate-controlled and stress-controlled simulations, inertial effects as evaluated through the reduced strain rate or *inertial number* I [2] should remain low enough. I is defined in terms of the mass m of a grain and characteristic stress σ as

$$I = \dot{\varepsilon}\sqrt{\frac{m}{a\sigma}}. \tag{4}$$

I values are requested not to exceed some upper bound $I^{\max}$: typically 10^{-3} in the first preparation stage, in which a granular gas is compressed to form the initial solid configuration; down to 10^{-4} or sometimes 10^{-6} in the subsequent quasistatic tests on the solid material. Suitable values are those for which the final results of interest no longer appreciably depend on strain rate.

Stresses are evaluated via the usual formula

$$\sigma_{\alpha\beta} = \frac{1}{V}\left[\sum_{i=1}^{N} m v_i^\alpha v_i^\beta + \sum_{1\leq i<j\leq N} F_{ij}^\alpha r_{ij}^\beta\right], \tag{5}$$

with a kinetic term (negligible except in the initial granular gas compression) involving velocities $\mathbf{v}_i$ of all N grains i within sample volume V, and a sum over pairs of interacting grains i, j transmitting force $\mathbf{F}_{ij}$ (from i to j) in their contact, $\mathbf{r}_{ij}$ denoting the "branch vector" pointing from the centre of i to the centre of j. As a result of (5), the average pressure $P = (\sigma_1 + \sigma_2 + \sigma_3)/3$ is simply connected to the average normal force in the contacts as

$$P = \frac{z\Phi\langle F_N\rangle}{\pi a^2}, \tag{6}$$

through the solid fraction Φ and the coordination number z. The dimensionless *stiffness number*, defined as

$$\kappa = \left(\frac{\tilde{E}}{P}\right)^{2/3}, \tag{7}$$

is such that the typical contact deflection h, relative to diameter a, is proportional to κ^{-1} (κ would be defined as K_N/aP with constant contact stiffness K_N, for linear contact elasticity). Using (6), the coefficient can be made explicit:

$$\langle (\frac{h}{a})^{3/2} \rangle^{2/3} = \left(\frac{3\pi}{z\Phi} \right)^{2/3} \kappa^{-1}. \tag{8}$$

2.3 Stiffness Matrices and Tensor of Elastic Moduli

Elastic moduli express the relations between small stress increments $\Delta \underline{\underline{\boldsymbol{\sigma}}}$ and small strains $\underline{\underline{\boldsymbol{\varepsilon}}}$, assuming the contact network, in equilibrium, behaves like a network of elastic springs, with stiffnesses K^N and K^T varying from contact to contact according to relations (2) and (3). This assumes that the effects of the mobilization of friction, which implies a non-elastic contact behaviour, are macroscopically negligible for small strain increments about the investigated equilibrium state, which needs to be checked. Stiffness matrices and their structure are presented and discussed in Refs. [36, 38, 48], and will not be detailed here.

At the macroscopic scale, in the oedometric and triaxial compressions considered here, the granular material is transversely isotropic, i.e., invariant by rotation about the major compression axis (index 1). The moduli are then defined by the following macroscopic relation between stress increments and small strains about an equilibrium prestressed state:

$$\begin{bmatrix} \Delta\sigma_{11} \\ \Delta\sigma_{22} \\ \Delta\sigma_{33} \\ \Delta\sigma_{23} \\ \Delta\sigma_{31} \\ \Delta\sigma_{12} \end{bmatrix} = \begin{bmatrix} C_{11} & C_{12} & C_{12} & 0 & 0 & 0 \\ C_{12} & C_{22} & C_{23} & 0 & 0 & 0 \\ C_{12} & C_{23} & C_{22} & 0 & 0 & 0 \\ 0 & 0 & 0 & 2C_{44} & 0 & 0 \\ 0 & 0 & 0 & 0 & 2C_{55} & 0 \\ 0 & 0 & 0 & 0 & 0 & 2C_{55} \end{bmatrix} \cdot \begin{bmatrix} \varepsilon_{11} \\ \varepsilon_{22} \\ \varepsilon_{33} \\ \varepsilon_{23} \\ \varepsilon_{31} \\ \varepsilon_{12} \end{bmatrix} \tag{9}$$

Equation (9) uses the *Voigt notation*, in which $\Delta \underline{\underline{\boldsymbol{\sigma}}}$ and $\underline{\underline{\boldsymbol{\varepsilon}}}$ are written as 6-dimensional vectors, and the elastic moduli form a second-rank tensor, denoted as $\underline{\underline{\mathbf{C}}}$, with corresponding indices, e.g., C_{11} for C_{1111}, or C_{44} for C_{2323}. Isotropy within the transverse plane (2, 3) entails

$$C_{22} - C_{23} = 2C_{44}. \tag{10}$$

In the isotropic case, there are only two independent elastic coefficients, the bulk modulus B and one shear modulus G, and the moduli written in Eq. (9) satisfy $C_{11} = C_{22} = B + 4G/3$, $C_{12} = C_{13} = C_{23} = B - 2G/3$, $C_{44} = C_{55} = G$. In anisotropic systems in which the tensor of elastic moduli has the transversely

isotropic symmetry of (9), a bulk modulus can be defined from the variation of average pressure with an applied, isotropic, volumetric strain, as

$$B = \frac{1}{9}\left(C_{11} + 4C_{12} + 2C_{22} + 2C_{23}\right). \tag{11}$$

3 Stress-Strain Relations and Material State: DEM Observations

This section provides a brief review of some basic features of material behaviour, which are observed and studied by DEM simulations of model systems, outside the elastic regime [37, 39, 40, 42]. Simulations are also used to correlate such macroscopic observations to state variables characterizing the material on the microscopic scale of the grains and the contact network.

3.1 Assembling Grains into Solid Packs

The first solid states are made under low stress on compressing granular gases to equilibrium. By varying either the friction coefficient in the granular compression stage (e.g., setting it to zero) or by mimicking numerically the effects of strong vibrations in dense states, it is possible to produce

(i) very dense, highly coordinated states denoted as A in the isotropic compression study, or DH (dense, high coordination number) in the oedometric compression study;
(ii) very dense, poorly coordinated states, denoted as C (isotropic compression) or DL (dense, low coordination) in the oedometric compression study;
(iii) looser states, referred to as D if isotropically compressed, or LL (loose with low coordination) in the oedometric test study.

The solid fraction Φ in very dense samples (A, C, DH, DL), initially assembled on setting the friction coefficient to zero, is the "random close packing" value $\Phi \simeq 0.64$. The (rattler-corrected) coordination number z^* of well-coordinated samples (A, DH) is near 6, while it decreases to about 4.6 in poorly coordinated ones. The rattlers, grain carrying no force, are very few in highly coordinated systems, but comprise typically 10% of all grains in poorly coordinated ones. Coordination number z becomes $z^* = z/(1 - x_0)$ as rattlers are excluded from the evaluation of the average number of contacts per grain. In addition (iv), intermediate states B were created using a small friction coefficient in the assembling stage, with $\Phi_B \simeq 0.628$ and $z_B \simeq 5.8$—thus looser than C but better coordinated— to further illustrate the independent variations of z and Φ in dense configurations.

The samples that were prepared for oedometric compression were assembled by isotropically or oedometrically compressing the initial granular gas, which duplicates each initial state: DHi/DHo, DLi/DLo, LLi/LLo. The nature of the gas compression does not significantly affect the density and the coordination number, but of course "o" states are anisotropic from the start, while "i" ones gradually become anisotropic in the oedometric compression process.

Finally, we also exploit a set of loose initial isotropic configurations, simply denoted as "L", with $\Phi = 0.571 \pm 0.005$ and $z^* \simeq 4.7$, as obtained from a compression cycle applied to initially wet beads, with a model of capillary cohesion—the liquid menisci being removed in the final state [49].

3.2 *Changing Stress Intensity: Isotropic and Oedometric Compressions*

We first discuss the elastic properties of systems subjected to large variations of stress intensities, without or with comparatively little change in stress directions.

Density and Coordination

States A, B, C, D are isotropically compressed up to large values of confining pressure P (100 MPa). The grains are assumed not to undergo any damage, despite the very large stress levels involved in their contacts [37]. States DH, DL and LL are similarly subjected to oedometric compressions, with σ_1 reaching 30 MPa. Such compression processes impose an increase of the solid fraction and of contact deflections, and consequently strongly depend on contact elasticity, which sets the scale of strains, determined by κ^{-1}. As κ (defined with P in (7) for isotropic compression, with σ_1 for oedometric compression) decreases from order 10^4–10^5 down to $\kappa \sim 100$ during compression, Φ typically increases by 2 to 5×10^{-2}. Meanwhile, coordination number z increases and rattler fraction x_0 decreases, as shown in Fig. 1, for the different systems subjected to oedometric compression. Note however that the coordination number, if initially high (as for DHo and DHi), does not increase monotonically with axial stress in oedometric compression.

Force Distribution and Friction Mobilization

The distribution of normal force values, regarded as characteristic of granular disorder, has been quite extensively studied in equilibrated granular assemblies [50–53]. It usually exhibits an exponential decrease of the probability density for large force values, and its width tends to vary with coordination number, the wider the smaller the contact density. Upon increasing the pressure in compressive loading,

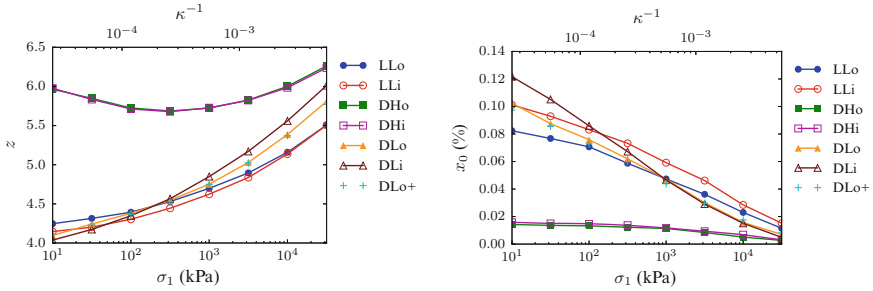

Fig. 1 Coordination number z (left graph) and rattler fraction x_0 (right graph) versus axial stress σ_1, or κ^{-1}, in oedometric compression of the different initial states ("DLo+" data pertain to DLo-type sample with 13,500 grains instead of 4000, showing size independence)

the coordination number increases and the force distribution becomes correlatively narrower [37, 54]. In the context of the estimation of stiffnesses and elastic moduli, force distributions are usefully characterized by their reduced moments, defined as

$$Z(\alpha) = \frac{\langle F_N^\alpha \rangle}{\langle F_N \rangle^\alpha}. \tag{12}$$

Thus the average contact stiffness, from Eq. (2), is related to $Z(1/3)$, which varies between 0.92 and 0.96 in the set of investigated bead packs. The width of the large force wing of the distribution may be assessed, e.g., from the values of $Z(2)$, which vary between 1.45 and 1.65.

A related quantity (close to $Z(5/3)$) is useful to evaluate elastic energies from contact forces. If r_{TN} is the ratio $\dfrac{||\mathbf{F_T}||}{F_N}$ in any contact, and α_T denotes the stiffness ratio K_T/K_N (see Eqs. (2) and (3)), then we define

$$\tilde{Z}(5/3) = \frac{\langle F_N^{5/3}(1 + \frac{r_{TN}^2}{\alpha_T}) \rangle}{\langle F_N \rangle^{5/3}}. \tag{13}$$

Values of $\tilde{Z}(5/3)$ are observed to vary between 1.1 and 1.4.

Friction mobilization is systematically larger in contacts carrying small normal forces [36, 37], and, globally, larger in scarcely coordinated systems. In oedometric compression, it is (surprisingly) larger in contacts with normal direction transverse to the major compression axis [42].

Anisotropy

Anisotropy is introduced in the assembling stage in systems DHo, DLo, LLo, for which the granular gas is assembled in solid form by oedometric compression. It

is gained in the course of compression for initially isotropic systems DHi, DLi, LLi or A to D. The simplest characteristics of anisotropy are the coefficients of the distribution of unit normal vector orientations and the angular distribution of normal force intensities. Defining angle θ between direction 1 and normal unit vector $\mathbf{n}$, with $0 \leq \theta \leq \pi$, the orientation distribution (or *fabric*) anisotropy is conveniently expressed by the probability density function (p. d. f.) of $\cos\theta = n_1$ over interval $-1 \leq n_1 \leq 1$, $p(n_1)$. By construction, it is an even function ($\mathbf{n}$ and $-\mathbf{n}$ are equivalent), constant with value $1/2$ in an isotropic system. $p(n_1)$ might be expanded in the series of Legendre polynomials, with only terms of even order. Truncating the series after the term of order 4, one has

$$p(n_1) = 1 + A_2\left(3n_1^2 - 1\right) + A_4\left(35n_1^4 - 30n_1^2 + 3\right), \tag{14}$$

in which coefficients are related to moments of the distribution: thus coefficient, A_2, given by

$$A_2 = \frac{15}{4}\left(\langle n_1^2\rangle - \frac{1}{3}\right) = \frac{15}{4}\int_{-1}^{1} p(n_1)n_1^2 dn_1 - \frac{5}{4}, \tag{15}$$

is directly related to the difference between the second moment and its isotropic value, for which we introduce the notation

$$\tilde{c}_2 = \langle n_1^2\rangle - \frac{1}{3}. \tag{16}$$

Figure 2 shows that the distribution of contact orientations (normalized, using $P(|n_1|) = 2p(n_1)$, such that the integral from 0 to 1 equals unity) is well fitted with relation (14), with coefficient A_4 given by

$$A_4 = \frac{9}{64}\left(35\langle n_1^4\rangle - 30\langle n_1^2\rangle + 3\right). \tag{17}$$

Figure 3 shows the evolution of $\tilde{c}_2$ in oedometric compression. We denote as $\mathcal{F}(\mathbf{n})$ the average normal force amplitude for contacts with normal direction $\mathbf{n}$, normalized by the global average $\langle F^N\rangle$, such that its integral over the unit sphere, Σ, weighed by the orientation distribution $p(\mathbf{n})$, satisfies

$$\int_{\Sigma} p(\mathbf{n})\mathcal{F}(\mathbf{n})d^2\mathbf{n} = 1. \tag{18}$$

Similarly to $p(\mathbf{n})$, $\mathcal{F}$, a function of $|n_1|$ may be expanded in a series of Legendre polynomials. We define

$$\tilde{f}_2 = \frac{1}{4\pi}\int_{\Sigma} \mathcal{F}(|n_1|)n_1^2 d^2\mathbf{n} - \frac{1}{3}, \tag{19}$$

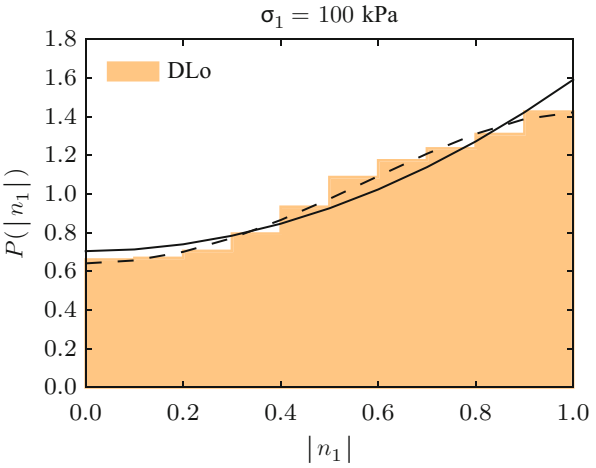

Fig. 2 Anisotropy of contact orientations: histogram of $|n_1|$ values in system DLo at $\sigma_1 = 100$ kPa, and its representation with expansion (14), truncated after order 2 (solid line) or order 4 (dashed line)

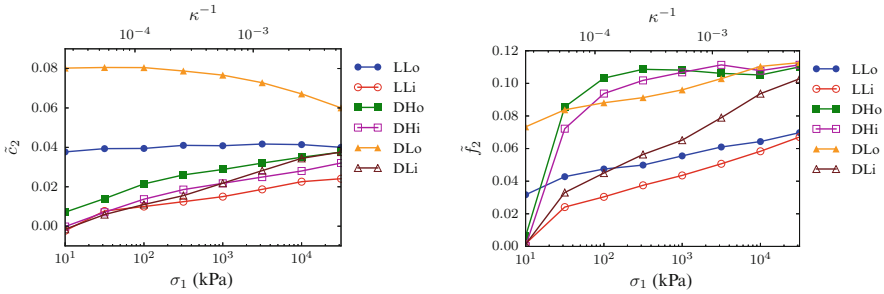

Fig. 3 Fabric anisotropy parameter $\tilde{c}_2$ and force anisotropy parameter $\tilde{f}_2$ versus axial stress σ_1 or κ^{-1} in oedometric compression of the different initial states

which vanishes in isotropic systems (Fig. 4).

Stress anisotropy in oedometric compression is characterized by the ratio of lateral to axial stresses $K_0 = \sigma_2/\sigma_1 = \sigma_3/\sigma_1$, traditionally referred to as the coefficient of earth pressure at rest [55, 56]. Stress components relate, in good approximation, to $\tilde{c}_2$ and $\tilde{f}_2$ [31, 41, 42, 57]. Ignoring the (very small) contribution of tangential forces to principal stresses in oedometric compression, one obtains

$$K_0 = \frac{2 - 3(\tilde{c}_2 + \tilde{f}_2)}{2 + 3(\tilde{c}_2 + \tilde{f}_2)}. \tag{20}$$

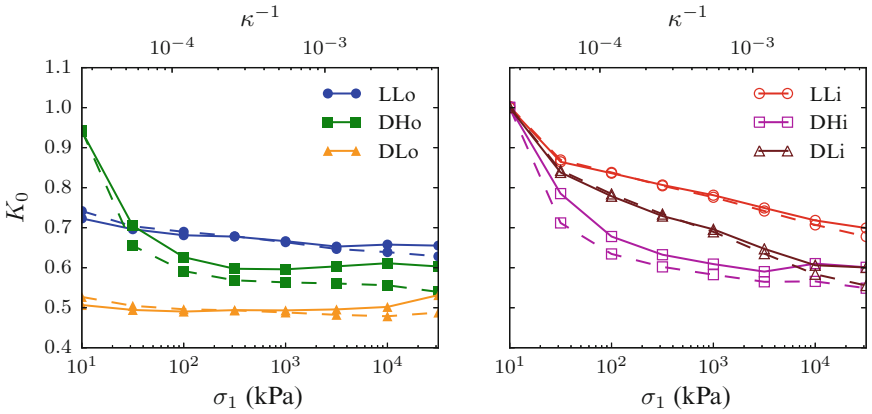

Fig. 4 Dots joined by solid lines: K_0 versus axial stress or κ^{-1} in oedometric compression. Dots joined by dashed lines: K_0 approximated by Eq. (20)

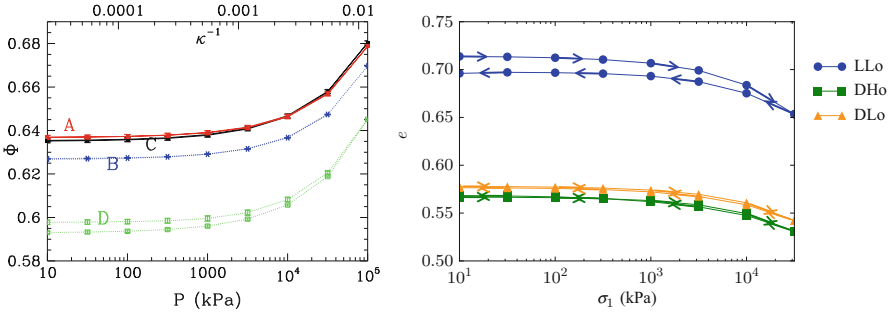

Fig. 5 Left: variations of solid fraction Φ in isotropic compression cycle for states A, B, C and D. Right: variations of void ratio e (see Eq. (21)) in oedometric compression cycle for states LLo, DLo and DHo

Unloading and Irreversibility

The increase in density under isotropic compression is, in appearance, very nearly reversed and cancelled upon reducing the pressure back to its initial value, as shown in Fig. 5. Remarkably, the small initial difference in solid fraction between states A and C (the latter being very slightly less dense) survives a loading cycle in which the pressure varies by 4 orders of magnitude. Only the looser state D exhibits a notable density change. Similar observations are made in oedometric compression, in which case, to conform to soil mechanics tradition, the *void ratio*, i.e.,

$$e = \frac{1 - \Phi}{\Phi}, \tag{21}$$

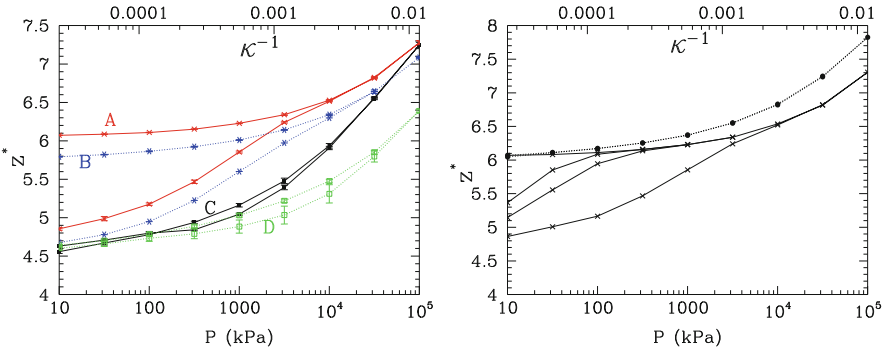

Fig. 6 Left: variations of rattler-corrected coordination number z^* in isotropic compression cycle for states A to D. Right: effects on z^* of smaller pressure cycles in A systems, with load reversals at 316.2 kPa, 3.162 MPa and 31.62 MPa, instead of 100 MPa

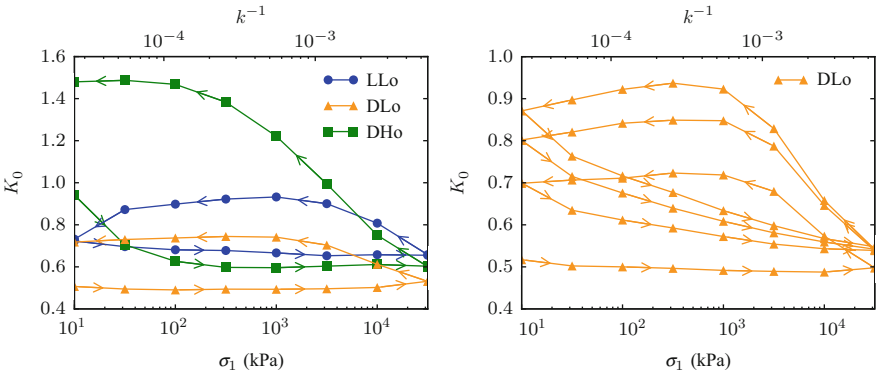

Fig. 7 Left: variations of stress ratio K_0 in oedometric compression cycle for states LLo, DLo and DHo. Right: effect of 3 repeated cycles on K_0 in state DLo

is plotted versus axial stress σ_1 on a logarithmic scale in Fig. 5 (right). As in the isotropic case, the small differences in initial densities are retrieved after a compression cycle in which stresses vary by more than 3 orders of magnitude, and a change in density is only notable in the loosest initial state (LLo).

Coordination numbers, on the other hand, do change over such a cycle, especially in the initially highly coordinated systems, in which the number of contacts is considerably decreased. This is shown in the isotropic compression case in Fig. 6.

Similar observations are made in oedometrically compressed systems, with coordination numbers, if initially large, as in systems DHi and DHo, reduced to smaller values the larger the loading cycle in terms of axial stress σ_1. Furthermore, this lack of reversibility is also extremely conspicuous for stress ratio K_0, the evolution of which on the unloading branch of the cycle, as shown in Fig. 7, is quite different from the one on the loading branch. The effect of the oedometric

loading cycle, in systems with small initial stress anisotropy (such as DHo, as well as initially isotropic systems DHi, DLi, LLi) is such that the stresses become larger in horizontal directions than along the compression axis, with $K_0 > 1$, up to about 1.5. This lack of reversibility rules out an elastic response in compression. In view of the subsequent behaviour under repeated load cycles (see right graph in Fig. 7), the unloading part of the cycle is also irreversible and anelastic. This conclusion is apparently at odds with the elastic-plastic compression laws often adopted in soil mechanics treatises, according to which the compression, both in isotropic and oedometric cases, should be plastic (irreversible) for growing stress levels but reversible and "elastic" on the unloading branch of the cycle, and as long as the maximum loading level the maximum has known in the past (the maximum pressure in isotropic compression), termed "preconsolidation stress", is not exceeded. We attribute this discrepancy to the frequent grain breakage or contact damage experienced by irregular sand grains under growing pressure, which is ignored in the numerical model. Such phenomena naturally explain the strong dissymmetry between loading and unloading, and are very likely to entail larger irreversibilities than the ones observed in DEM with elastic-frictional grains without damage in the contacts.

Another remarkable feature of the simulated isotropic or oedometric compression tests investigated in the model systems discussed here is the enduring memory of the initial assembling procedure kept in the internal states of the different systems despite the large increase of the applied stresses. The different initial configurations do not approach the same state under large pressure or axial stress.

3.3 Changing Stress Direction: Triaxial Compression

Axisymmetric triaxial compression (Fig. 8) is the most classical mechanical test probing the shear strength of a granular material in controlled stress conditions [6]. In the most frequent experimental configuration, as schematized in Fig. 8, it consists in subjecting a cylindrical specimen, maintained under constant lateral pressure $\sigma_2 = \sigma_3 = P_0$, to a vertical stress σ_1 gradually growing from initial value P_0. The principal stress values thus evolve from the initial isotropic state $\sigma_1 = \sigma_2 = \sigma_3 = P_0$ to growing values of deviator stress $q = \sigma_1 - \sigma_3 = \sigma_1 - \sigma_2$, maintaining the same symmetry of revolution as in the oedometric test. Results of the triaxial compression test are traditionally expressed as the dependence of *deviator stress* $q = \sigma_1 - \sigma_3$ and of the *volumetric strain* $\varepsilon_v = \varepsilon_1 + \varepsilon_2 + \varepsilon_3$ on the axial strain, $\varepsilon_a = \varepsilon_1$. (For large strains, keeping the simple definition of $\varepsilon_1, \varepsilon_2, \varepsilon_3$ as relative length reductions along the principal axes, open should use the definition $\varepsilon_v = 1-(1-\varepsilon_1)(1-\varepsilon_2)(1-\varepsilon_3)$). The growth of $-\varepsilon_v$, expressing material dilation, with ε_a is the dilatancy of the granular material under deviatoric (shear) strain.

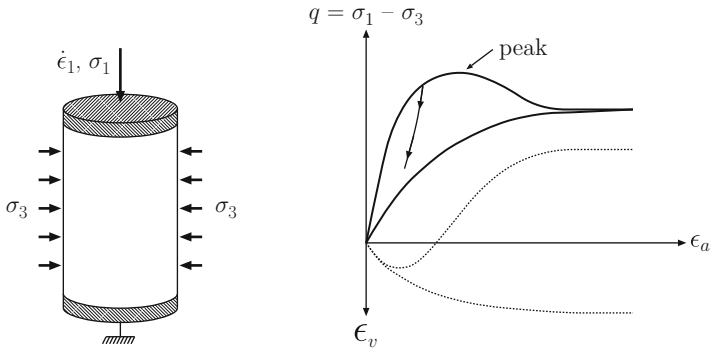

Fig. 8 Left: schematic view of triaxial compression test. Right: aspect of deviatoric stress q (solid line) and volumetric strain ε_v (thin dotted line) versus axial strain $\varepsilon_a = \varepsilon_1$ for initially dense (upper curves for both q and $-\varepsilon_v$) and loose (lower curves) states

Approach to the Critical State for Large Strains

A fundamental property of quasistatic granular mechanics is the existence of *critical states*, attractor states approached by the material subjected to monotonically growing strain, irrespective of the initial state. Thus under growing axial strain ε_a in triaxial compression, the material achieves a certain deviator stress level, as well as values of density and internal structure parameters, independent of its initial preparation. As sketched in the second graph of Fig. 8, initially dense samples first slightly contract, and then dilate. The deviator stress, in those systems, first grows, then passes through a maximum (the "peak" deviator stress) and then decreases to a plateau. In initially loose systems, both q and solid fraction Φ monotonically increase to the same asymptotic values as in the dense case.

Lots of DEM studies were devoted to the investigation of the critical state and characteristic internal state parameters approaching the corresponding critical values [58–62]. Typical results [39] are shown in Figs. 9 and 10. Figure 9 shows the evolution of deviator stress and solid fraction, both quantities approaching their asymptotic critical values for $\varepsilon_a \geq 0.25$, irrespective of their initial structure. The approach of internal variables to specific critical values is visualized in Fig. 10. Note that the same value $\tilde{c}_2 = \langle n_1^2 \rangle - 1/3 \simeq 0.07$ for large strains is obtained in both graphs, and thus for all three initial states A, D and L.

4 Elastic Properties in Isotropic or Oedometric Compression

We now turn to the investigation of elastic response in the case of the compression tests of Sect. 3.2, either isotropic or oedometric, in which stresses mostly change in intensity, over several decades.

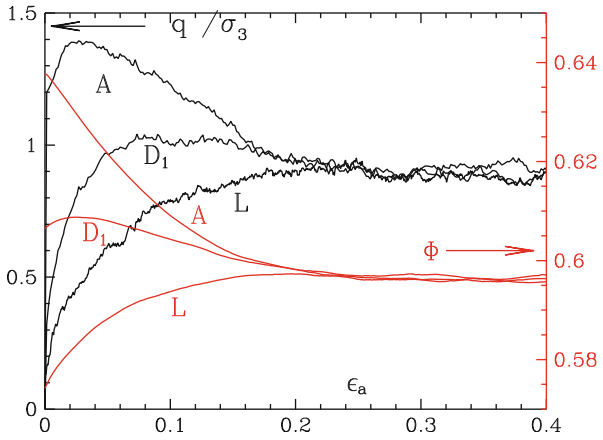

Fig. 9 Deviator stress q and solid fraction Φ versus axial strain ε_a in simulated triaxial tests ($P_0 = 100\,\text{kPa}$ or $\kappa \simeq 8000$) carried out with initial states A, D and L

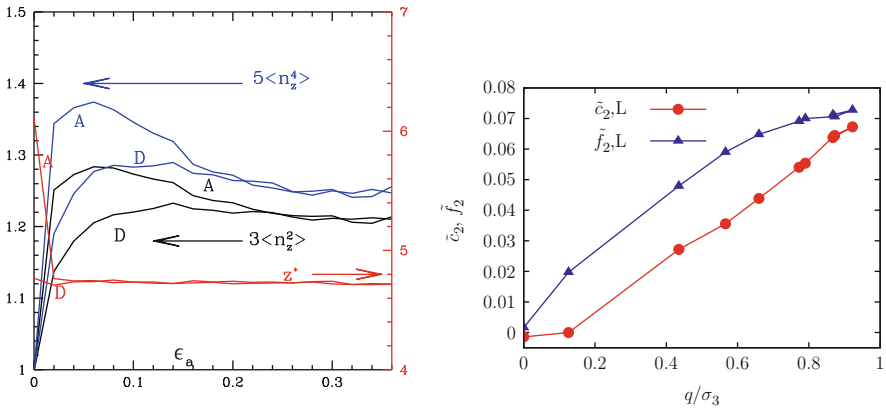

Fig. 10 Left: evolution of coordination number z^* and fabric parameters (here $n_z = n_1$) in dense and medium dense systems A and D in triaxial compression test, versus ε_a. Right: increase of anisotropy parameters $\tilde{c}_2$ and $\tilde{f}_2$ (see Eqs. (16) and (19)) in loose system L, versus normalized deviator q/σ_3

4.1 Moduli in Isotropic Compression

Under growing isotropic or oedometric load, contact stiffnesses (see Eqs. (2) and (6)) scale as $(z\Phi)^{-1/3} P^{1/3}$, while the density of contacts is proportional to $z\Phi$, whence an expected scaling for elastic moduli C:

$$C \sim (z\Phi)^{2/3} P^{1/3}. \tag{22}$$

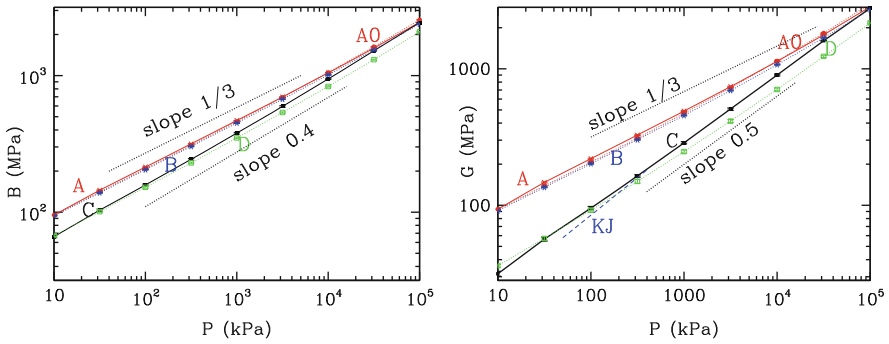

Fig. 11 Bulk (left) and shear (right) moduli versus confining pressure on doubly logarithmic scale in isotropic compression of states A, B, C, D. Line marked "KJ": fit through experimental data of Ref. [9]

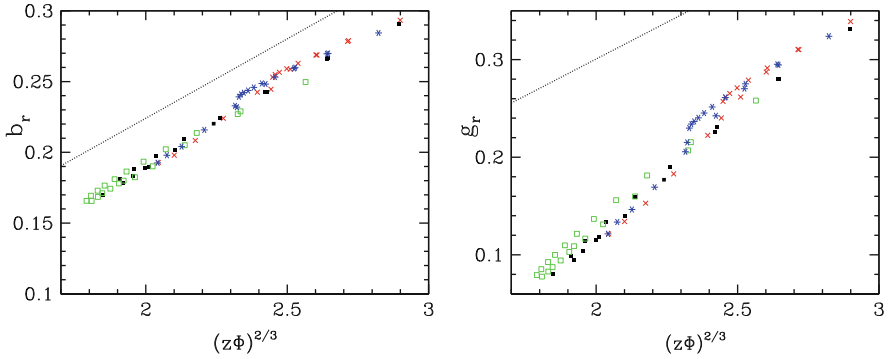

Fig. 12 Left: reduced bulk modulus $b_r = B/(\tilde{E}^{2/3}P^{1/3})$, for systems A to D in compression cycle, versus $(z\Phi)^{2/3}$. Right: same graph for reduced shear modulus $g_r = G/(\tilde{E}^{2/3}P^{1/3})$. Dotted lines show Voigt predictions

Figure 11 shows the evolution of bulk and shear moduli, computed for a set of intermediate equilibrium states, versus confining pressure in isotropically compressed systems A to D (among which intermediate system B is less dense than C, with $\Phi_B \simeq 0.625$, but more coordinated, $z_B^* \simeq 5.8$). It is immediately apparent that moduli primarily depend on coordination number, as moduli in poorly coordinated systems C and D, despite their different densities, nearly coincide, and significantly differ from those in well-coordinated systems A and B. To some extent, this is explained by the predicted scaling with $(z\Phi)^{2/3}$, since coordination number z (from 4 to 6 at low pressure) differs more than solid fraction Φ (from 0.6 to 0.64 at low pressure) between the different preparation procedures. This scaling is however imperfectly satisfied, as shown in Fig. 12. While the bulk modulus approximately abides by the behaviour expected from (22), the shear modulus increases significantly faster with z.

4.2 Estimating Elastic Moduli

Voigt Estimates By analogy with elasticity of heterogeneous continuous media, we refer as *Voigt estimates* to the approximate values of elastic moduli obtained from the assumption of homogeneous strains, which in the case of a discrete granular assembly amounts to assuming that grain centres move like the points of a homogeneous elastic medium. As in the continuous case, it can be shown [38] that the resulting estimated bulk and shear moduli are upper bounds to the true values. In the isotropic case, one obtains (superscript V denotes Voigt estimates, and $Z(1/3)$ is defined in Eq. (12)):

$$\begin{aligned} B^{\mathrm{V}} &= \frac{Z(1/3)}{2}\left(\frac{z\Phi\tilde{E}}{3\pi}\right)^{2/3} P^{1/3} \\ G^{\mathrm{V}} &= \frac{6+9\alpha_T}{10} B^{\mathrm{Voigt}}. \end{aligned} \tag{23}$$

The Voigt estimates for the five moduli defined in Eq. (9) are obtained analogously. Let us introduce notations $f_N = F_N/\langle F_N\rangle$ for the normal contact force divided by its average, $\alpha_T = K^T/K^N = (2-2\nu)/(2-\nu)$ (see Eq. (3)) for the ratio of tangential to normal contact stiffnesses, and C_0, for the following factor (involving contact density and typical contact stiffness):

$$C_0 = \frac{3^{4/3}}{2\pi^{2/3}}(z\Phi)^{2/3}\tilde{E}^{2/3}P^{1/3}. \tag{24}$$

Then, defining the following averages for any coordinates α, β of unit normal vector $\mathbf{n}$,

$$\mathcal{A}_\alpha = \langle f_N^{1/3} n_\alpha^2\rangle; \quad \mathcal{B}_{\alpha\beta} = \langle f_N^{1/3} n_\alpha^2 n_\beta^2\rangle, \tag{25}$$

Voigt estimates of elastic moduli read (no summation implied over repeated indices)

$$C^{\mathrm{V}}_{\alpha\alpha} = C_0\left[(1-\alpha_T)\mathcal{B}_{\alpha\alpha} + \alpha_T\mathcal{A}_\alpha\right] \quad (1 \le \alpha \le 3) \tag{26}$$

$$C^{\mathrm{V}}_{\alpha\beta} = C_0(1-\alpha_T)\mathcal{B}_{\alpha\beta} \quad (1 \le \alpha < \beta \le 3) \tag{27}$$

$$C^{\mathrm{V}}_{44} = C_0\left[(1-\alpha_T)\mathcal{B}_{23} + \frac{1}{2}\alpha_T\mathcal{A}_3.\right] \tag{28}$$

Optimal Voigt estimates of moduli involve [38, 63, 64] a common spin to all particles, which vanishes if the strain tensor has common eigendirections with the

fabric tensor $\underline{\underline{\mathbf{F}}}$, defined as $F_{\alpha\beta} = \langle n_\alpha n_\beta \rangle$. In the present case of transverse isotropic media this only affects shear modulus C_{55}, resulting in formula

$$C_{55}^{\mathrm{V}} = C_0 \left[(1 - \alpha_T)\mathcal{B}_{12} + \alpha_T \frac{\mathcal{A}_1 \mathcal{A}_2}{\mathcal{A}_1 + \mathcal{A}_2} \right]. \tag{29}$$

Relations (23) and (24) abide by the expected scaling (Eq. (22)). As to quantitatively estimating the values of moduli, Fig. 12 shows that, although B is only slightly overestimated in isotropic systems, Voigt predictions of shear moduli can be much larger than actual values for poorly coordinated systems. Turning to anisotropic, oedometrically compressed systems, similar observations can be made: the bulk modulus, as expressed in (11), is not sensitive to the varying degree of anisotropy between the different states, and only distinguishes highly coordinated (DH) from poorly coordinated (DL and LL) states, as shown in Fig. 13. As in the isotropic case, the Voigt estimate B^{V} only exceeds the true value of B by less than 15%. On the other hand, as shown in the second plot of Fig. 13, the shear moduli are grossly overestimated by the Voigt approximation, the more the lower the coordination number, ratio G^{V}/G reaching 3.5 in the worst case, state DLo under low axial stress.

Reuss Estimates Just like in elasticity of heterogeneous continua, it is possible in principle to write down upper bounds to elastic compliances using trial values of contact force increments balancing applied stress increments. Such trial forces are, however, not known in general, except in the special case of stress increments proportional to the preexisting stresses. One may then, as described in Ref. [38], exploit the knowledge of the distribution of forces to write an estimate of one specific elastic compliance, expressing the response to a change in stress intensity for the same stress direction. Assuming transverse isotropy as in the oedometric or triaxial compression tests, elements of the 3×3 upper left block of the compliance

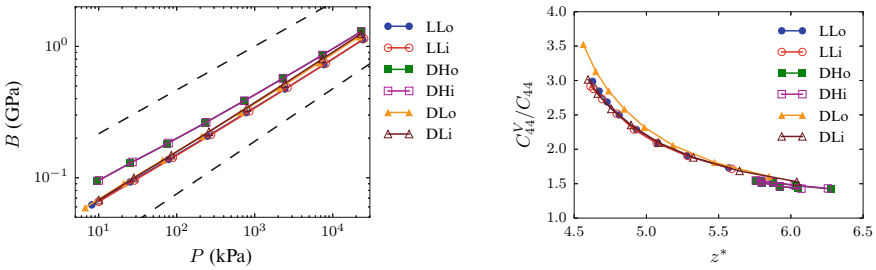

Fig. 13 Left: bulk modulus, as defined in Eq. (11), under oedometric compression cycle, versus average pressure in different systems subjected to oedometric compression. Dashed line slopes: 1/3 (top), 0.4 (bottom). Right: ratio $C_{44}^{\mathrm{V}}/C_{44}$ versus rattler-corrected coordination number z^* in oedometric compression

matrix (the inverse to the matrix written in Eq. (9)) are usually defined in terms of Young moduli E_1, E_2 and Poisson ratios ν_{12}, ν_{23} as

$$\underline{\underline{\tilde{\mathbf{M}}}} = \begin{bmatrix} \frac{1}{E_1} & \frac{-\nu_{12}}{E_1} & \frac{-\nu_{12}}{E_1} \\ \frac{-\nu_{12}}{E_1} & \frac{1}{E_2} & \frac{-\nu_{23}}{E_2} \\ \frac{-\nu_{12}}{E_1} & \frac{-\nu_{23}}{E_2} & \frac{1}{E_2} \end{bmatrix}. \tag{30}$$

Specifically, in the transversely symmetric case, denoting as K_0 the stress ratio as in Sect. 3.2, a Reuss estimate might be written for the following compliance:

$$S_P = \frac{1 - 4\nu_{12}K_0}{E_1} + \frac{2(1-\nu_{23})K_0^2}{E_2}, \tag{31}$$

as [38, 41]

$$S_P^R = 2\left(\frac{3\pi}{z\Phi}\right)^{2/3} \frac{\tilde{Z}(5/3)}{\tilde{E}^{2/3}P^{1/3}}. \tag{32}$$

In the isotropic case $1/S_P^R$ provides a lower bound to B, which only differs from B^{V}, as written in (23), by factors of order 1 related to the shape of the force distribution. This explains the success of the Voigt approximation for the bulk modulus in isotropic systems. In transversely isotropic ones, modulus B also turns out correctly estimated (within 15%) in our results [28]: it appears to be nearly equal to the bulk modulus of an isotropic system with the same coordination number. The error on S_P as predicted by the Reuss estimate is also of order 10% (16% in the worst case in [28]). Meanwhile, errors in Voigt-estimated shear moduli (see Figs. 12 and 13) are quite large, especially in poorly coordinated systems. Poisson ratios are also very poorly predicted [28, 38].

More Sophisticated Approaches La Ragione and Jenkins [65], in the isotropic case, designed an improved prediction scheme for elastic moduli, based on a self-consistent approach to the fluctuations (ignored in the Voigt approach) of local grain displacements about the average affine field, on the scale of a pair of contacting grains. The resulting formulae are quite complex and have not been generalized to anisotropic systems. They were observed to improve the prediction of shear moduli to some extent, although still not accurately in systems with low coordination number. The role of fluctuations was explored by numerical means [20, 66], with investigations of the scale over which a similar self-consistent scheme should become accurate [20].

The Singular Limit of Vanishing Force Indeterminacy The anomalously low values of elastic moduli in poorly coordinated granular systems, as observed in

numerical studies, have been related to the singular values of eigenfrequencies of stiffness matrices [22, 67]. Both phenomena are controlled by the approach of a state of vanishing force indeterminacy (or degree of hyperstaticity). Such a situation occurs in packings of frictionless objects in the rigid limit ($\kappa \to \infty$) [68], as often studied in numerical simulations of spherical bead assemblies [22, 36, 69, 70]. It was predicted in [24] that the singular moduli (the shear modulus in the isotropic case) should vary proportionally to the degree of force indeterminacy as this limit is approached. With frictionless beads, the degree of force indeterminacy H is directly related to coordination number z^*, as

$$\mathrm{H} = \frac{1}{2} n(1 - x_0)(z^* - 6), \tag{33}$$

in a system of n particles with rattler proportion x_0 [68]. In the presence of friction, one should in principle [36, 38] define a slightly corrected value of z^*, denoted as z^{**}:

$$z^{**} = z^* + \frac{2x_2}{3(1 - x_0)}, \tag{34}$$

where x_2 is the proportion of 2-coordinated beads. The degree of force indeterminacy is then given by

$$\mathrm{H} = \frac{3}{2} n(1 - x_0)(z^{**} - 4). \tag{35}$$

x_2 values raise to about 2.5% in configurations C and D discussed here, for which z^* on the order of 4.5 under low pressure still implies a notable force indeterminacy. $\mathrm{H} = 0$, in frictional systems, may be approached in simulations carried out in the (unrealistic) limit of very large friction coefficient ($\mu \to \infty$) [25, 36].

The prediction $G \propto \mathrm{H}/n$ is checked in Fig. 14, using a reduced shear modulus g_a obtained by dividing G by density and average contact stiffness. The vanishing of shear modulus proportionally to the force indeterminacy is very well satisfied in the frictionless case. With frictional beads, such a behaviour is retrieved in the infinite friction case (state Z on the figure), and approached in some poorly coordinated systems with a realistic value of μ. The linear fits through the data predict that the shear modulus should vanish for $z^* = 6$ for frictionless beads and $z^{**} = 4$ for frictional ones, and thus, from relations (33) and (35), for $\mathrm{H} = 0$. The self-consistent approach of La Ragione and Jenkins [65] does not capture this tendency. The results on modulus C_{44} in oedometrically compressed systems shown in Fig. 13 exhibit a similar vanishing tendency for the smallest values of z^* (evidenced by the growth of ratio $C_{44}^{\mathrm{V}}/C_{44}$).

Studies of frictionless systems under low pressure (in the rigid limit of large κ) [41, 71] reveal that, in general, all moduli tend to vanish with the degree of force

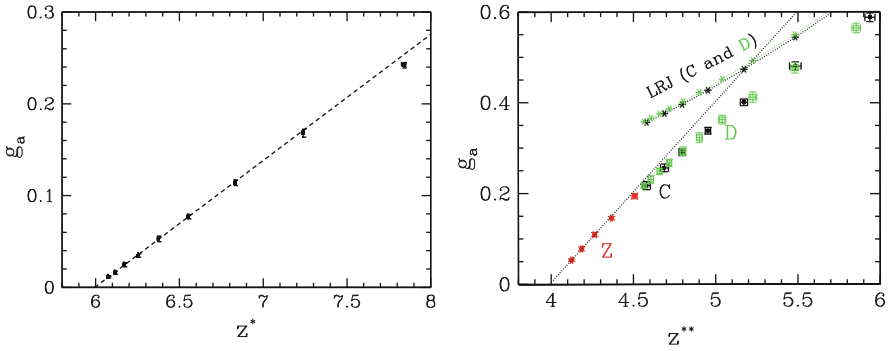

Fig. 14 Reduced shear moduli g_a versus corrected coordination number, in systems in isotropic compression. Left: frictionless case. Right: frictional case, with poorly coordinated states C and D, and state Z, assembled with infinite friction coefficient. z^{**} defined from z^* as in Eq. (34). Data points marked "LRJ": prediction of the La Ragione-Jenkins scheme [65]. Dotted lines: linear fits

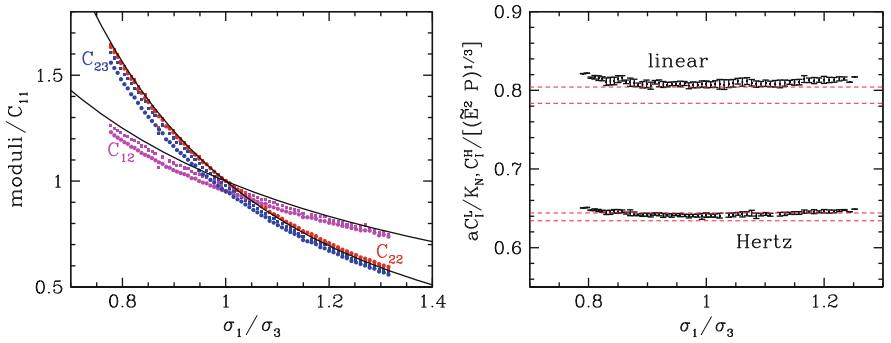

Fig. 15 Elastic moduli of nearly rigid frictionless bead packs under triaxial compression ($\sigma_1 \geq \sigma_2 = \sigma_3$) or extension ($\sigma_1 \leq \sigma_2 = \sigma_3$). Left: ratio of moduli to C_{11}, for Hertzian (square dots) or linear (round dots) contact elasticity. Continuous lines: behaviour predicted in Eqs. (36). Right: dominant eigenvalue C_I (data points) of tensor of elastic moduli, compared to Reuss prediction (between dashed lines) with Hertzian (C_I^H) or linear (C_I^L) contact elasticity

indeterminacy, except the one ($1/S_P$) associated with a proportional increase of all stress components, for which the Reuss estimate becomes exact [41] (see Fig. 15).

4.3 Anisotropy

The dominant feature in the variations of elastic moduli within the set of material states obtained through different preparation methods and subsequently subjected to oedometric compression is the role of coordination number—this is similar, as explained above, to the behaviour of isotropic systems. We now turn to specific

properties of transversely isotropic system, and briefly discuss the sensitivity of elastic moduli to fabric and force anisotropy parameters.

In the extreme case of nearly isostatic frictionless bead assemblies in the rigid limit [41], the one non-singular eigenvalue of the tensor of elastic moduli, playing the role of bulk modulus B in the isotropic case, is $1/S_P$, all the others becoming negligible in comparison. This implies the following relations between moduli:

$$\begin{aligned} \frac{C_{22}}{C_{11}} &\simeq \left(\frac{\sigma_{33}}{\sigma_{11}}\right)^2 \simeq \frac{C_{23}}{C_{11}} \\ \frac{C_{12}}{C_{11}} &\simeq \frac{\sigma_{33}}{\sigma_{11}}, \end{aligned} \tag{36}$$

a behaviour clearly satisfied by the data shown in Fig. 15. Remarkably, these relations, characteristic of a nearly singular tensor of moduli, with all eigenvalues vanishing except one, still hold on replacing the Hertzian contact elasticity by a linear unilateral law.

In the general case, assemblies of frictional beads under axisymmetric compression (oedometric or triaxial) depart from the singular limit of vanishing force indeterminacy, and their moduli, even though some are anomalously small (see Fig. 13, right graph), are sensitive both to fabric anisotropy and, because from (2) and (3), stiffnesses increase with forces, also to force anisotropy. The latter effect should be smaller in systems with small force indeterminacy H, and it vanishes for $\mathrm{H} = 0$, as the force values are then determined by the sole contact network geometry. Figure 16 shows the variations of the ratio of longitudinal moduli in oedometrically assembled systems. The Voigt prediction is inaccurate for these moduli, but it may provide a fair prediction of ratio C_{11}/C_{22} for moderately

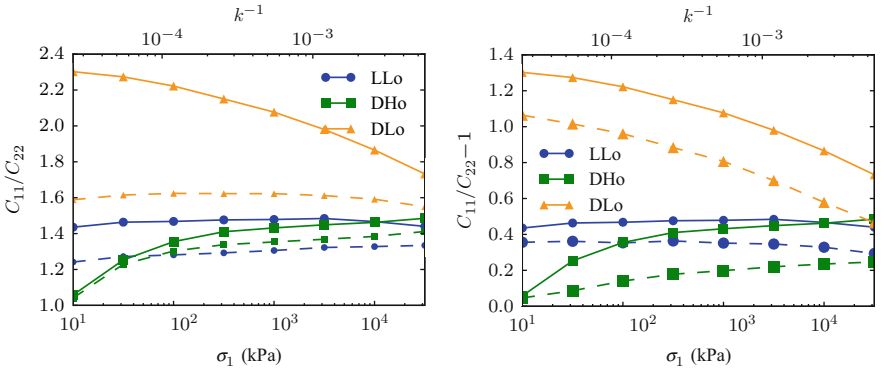

Fig. 16 Ratio, C_{11}/C_{22}, of longitudinal moduli in axial and lateral directions in oedometrically compressed transversely isotropic systems, versus axial stress (or κ^{-1}) in oedometric compression for different initial states. Dashed lines show Voigt prediction in left graph, results for linear contact elasticity in right graph

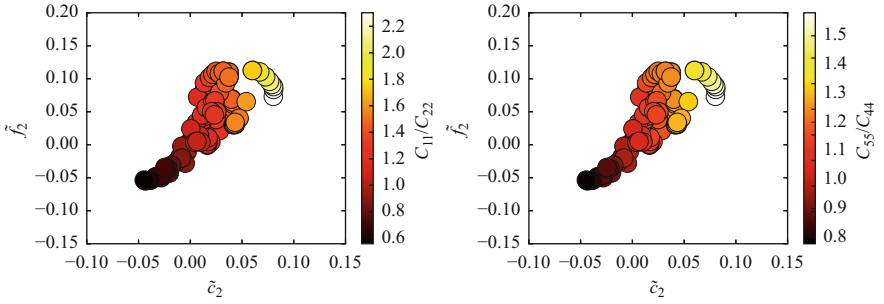

Fig. 17 Ratios of moduli characterizing elastic anisotropy: C_{11}/C_{22} (left) and C_{55}/C_{44} (right), with values encoded as colour intensity in $\tilde{c}_2$, $\tilde{f}_2$ plane

anisotropic, well-coordinated systems (DHo). However, it underestimates relative difference $C_{11}/C_{22} - 1$ by as much as 50% for large anisotropies (DLo) and/or small coordination numbers (DLo and LLo). On computing the moduli with linear contact elasticity, one keeps the effect of fabric anisotropy, but suppresses the one of force anisotropy. The second graph of Fig. 16 shows that the effect of force anisotropy, as expected, decreases for smaller force indeterminacies (in poorly coordinated systems). Then the anisotropy of the moduli appears to be primarily due to fabric anisotropy. This stronger effect of fabric, as opposed to force anisotropy, is also apparent on plots of elastic anisotropy, as characterized by the ratios of longitudinal moduli and of shear moduli, encoded as colour intensity, shown in Fig. 17, versus both anisotropy parameters $\tilde{c}_2$ and $\tilde{f}_2$. While it is not obvious in general to distinguish the effects of anisotropic fabric ($\tilde{c}_2$) from those of anisotropic forces ($\tilde{f}_2$), given that both vary in a correlated way, it does appear that the rightmost regions of the graphs contain lighter dots on going from top left towards the bottom right direction, implying a larger effect of fabric in the most anisotropic cases. Given that the Voigt approximation scheme, as shown in Fig. 16, proves again insufficient, we do not have any quantitative means to relate the force network anisotropy to the anisotropy of the tensor of elastic moduli. The results reported here nevertheless indicate qualitative trends and attainable orders of magnitude for elastic anisotropy among a series of states varying in density, coordination and initial fabric.

4.4 Anelasticity and Irreversibility: Elastic Range

We now compare the stresses (σ_1 and $\sigma_2 = K_0\sigma_1$)) versus strain ($\varepsilon_a = \varepsilon_1$) curves to the elastic response about an equilibrium state along the oedometric curve. It should be recalled that moduli are measured from stiffness matrices of contact networks, built on assimilating all contacts to elastic elements (involving normal and tangential stiffness constants, depending on the instantaneous value of the contact force). To obtain non-singular, well behaved matrices the system has to be carefully

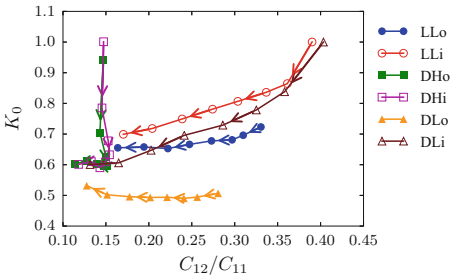

Fig. 18 Ratio of elastic moduli C_{12}/C_{22} versus stress ratio K_0 in oedometric compression (arrows indicating growing stress) for differently assembled samples

equilibrated, and it turns out, in practice, to suppress full friction mobilization in the contacts: the Coulomb inequality, in all contacts, is satisfied in the strict form, and no situation of incipient sliding is to be found anywhere in the contact network. If the equilibration is carried out under constant applied stress from an intermediate configuration reached along a strain rate-controlled compression path, it involves then an additional creep strain interval (typically of order 10^{-5} in the conditions of the simulations). Because of the role of friction in oedometric compression [42] the evolution is not elastic. In particular, as clearly shown in Fig. 18, the stress ratio K_0 systematically differs from the moduli ratio C_{12}/C_{11}. A nearly constant value of C_{12}/C_{11}, as in well-coordinated systems, over 3 decades of stress should imply a constant K_0 if the compression were elastic. A nearly constant K_0, as for LLo and DLo, should imply a constant C_{12}/C_{11}. This is contradicted by the results of Fig. 18.

The small elastic response after equilibration is similar to the one observed in experiments on sands [11, 72] after some creep strain (obtained by waiting a few hours). Even though the experimental creep, likely due to microcreep on the grain surfaces, as discussed, e.g., in Refs. [73, 74] and the numerical one (corresponding to the approach to equilibrium of a system subjected to much higher strain rates than in the laboratory) are of different physical origins, they entail similar effects: the system subsequently responds quasielastically, and the initial anelastic stress-strain curves are retrieved beyond a small strain domain. This is illustrated in Fig. 19.

The quasielastic domain, as identified in tests like the one of the first graph in Fig. 19, from the interval of strain ε for which the stress increment $\Delta\sigma$ differs from the elastic prediction $C\varepsilon$ by less than 5%, is observed to extend in the 10^{-6} or 10^{-5} range for the available data set, approximately growing with axial stress as $\sigma_1^{2/3}$. This power law corresponds to a constant relative stress increment $\Delta\sigma_1/\sigma_1$ for the quasielastic domain, assuming the modulus to grow as $\sigma_1^{1/3}$. This trend is apparent in Fig. 20. While oedometric unloading is sometimes regarded as elastic, it is observed here to be associated with irreversible evolutions, and the stresses, upon unloading, also depart from the elastic prediction after a strain interval larger than in the forward loading direction, but still of order 10^{-5} or 10^{-4}.

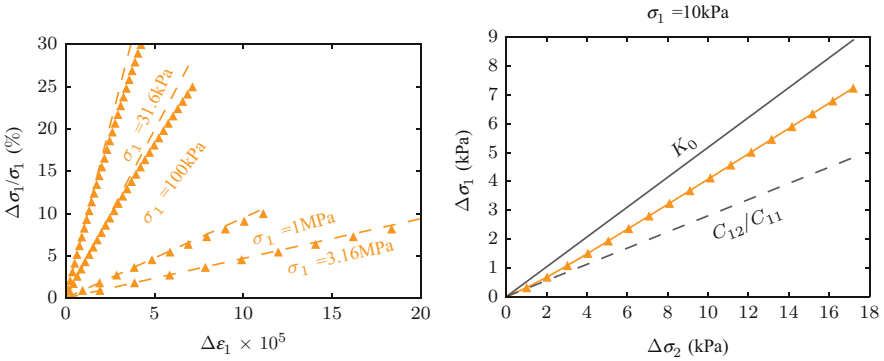

Fig. 19 Left: quasielastic range near equilibrated state along compression path of a sample of type DLo, for different values of axial stress σ_1. Straight lines have slopes C_{11}. Dots show stress-strain curves on resuming oedometric compression. Right: evolution of stresses from intermediate equilibrium. Slope of σ_2 versus σ_1 gradually evolves from C_{12}/C_{22} to K_0

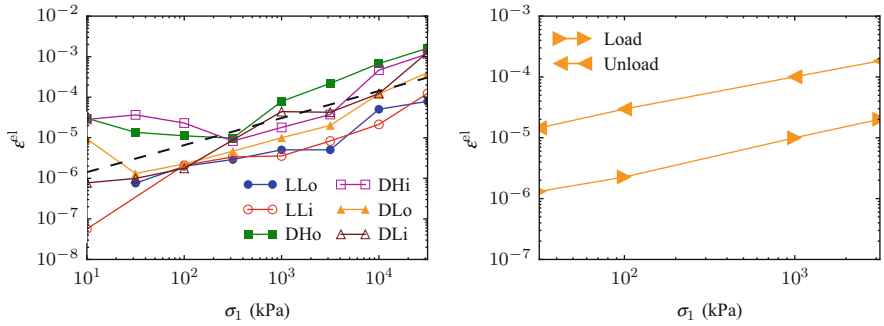

Fig. 20 Left: quasielastic range near equilibrated state along compression path of samples of different types, versus axial stress σ_1. Straight line has slope 2/3. Right: elastic domain in loading and unloading in states DLo

5 Elastic Properties in Triaxial Compression

In many respects, the evolution of a granular material under triaxial compression, as briefly described in Sect. 3.3, strongly differs from its evolution under the isotropic or oedometric compressions of Sects. 3.2 and 4. The direction of the stresses is changing, as opposed to their intensity. As the deviator level gradually increases, macroscopic failure is approached, as the fabric and force distribution in the rearranging contact network will prove unable to support the stresses. Such a failure is gradual as the critical state is approached from an initially loose configuration. It might be more sudden and catastrophic in initially dense systems, which should be unstable in deviator stress-controlled compression as the peak value is reached (other instabilities, associated with shear banding localisation, tend

to occur before the peak [75–77]). Do elastic properties detect incipient material failure (as speculated, e.g., in [34])? From the observations reported in the previous sections on the nature of elastic response and the conditions in which elastic moduli are measured, it transpires that the answer to this question should be negative. While elastic moduli are attached to one particular contact network, material failure is associated with the impossibility of rearranging the contact network in order to support larger deviatoric stresses.

In this section, we quickly review some results on the elastic moduli and their connections to internal state variables (Sect. 5.1), showing similar results as in Sect. 4. Then we discuss the role of contact stiffness and contact deflections in macroscopic strains (Sect. 5.2), and discuss the elastic or quasielastic range in Sect. 5.3.

5.1 Moduli and Internal State Parameters

Comparing Figs. 10 and 3, it is noteworthy that parameters $\tilde{c}_2$ and $\tilde{f}_2$, characterizing fabric and force anisotropy, reach similar values in triaxial compression of loose systems evolving to the critical state and in some samples under oedometric compression. Both L systems in triaxial compression and poorly coordinated ones (types DL and LL) in the early stages of oedometric compression also share similar coordination numbers (z^* between 4.5 and 4.8). Quite unsurprisingly, similar observations are also made on moduli in triaxial compression and under oedometric loading, as shown in Fig. 21. The ratio of longitudinal moduli in the major principal direction and in the transverse direction, C_{11}/C_{22}, grows along with anisotropy parameters, reaching 2 as anisotropy is maximized (compare with Fig. 16). The ratio $C_{44}^{\mathrm{V}}/C_{44}$ of the Voigt estimate of the shear modulus in the transverse plane to its exact value varies between 2 and 3, showing that C_{44} is anomalously low, as previously observed in all systems with low coordination. In general, all Voigt

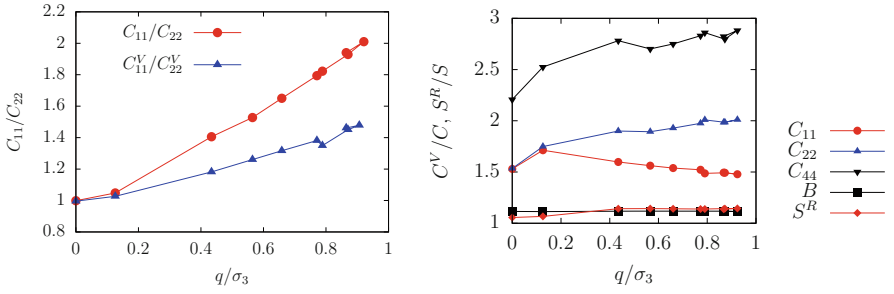

Fig. 21 Left: ratio of longitudinal moduli versus normalized deviator q/σ_3 in triaxial compression of loose systems (L), along with Voigt prediction. Right: ratios of Voigt predictions to measured moduli, and ratio S_P^R/S_P, versus q/σ_3

estimates perform poorly, except the bulk modulus as defined in (11). The Reuss estimate of compliance S_P, as defined in (31), is also quite correct. And, just like in the oedometric compression case, Voigt estimates also fail to predict ratios like C_{11}/C_{22} accurately. A similarly elastic anisotropy is observed in dense systems (such as A and C, see Sect. 3.1), for which ratio C_{11}/C_{22} grows from 1 to 2.5 in the pre-peak range (i.e., for $\varepsilon_a \leq 0.02$, see Fig. 9).

5.2 *Elasticity and Stress-Strain Curves*

An important difference between isotropic or oedometric compression (Sect. 3.2), on the one hand, and triaxial compression (Sect. 3.3), on the other hand, is the possibility to observe the evolution towards the characteristic behaviour of granular assemblies under shear or triaxial compression with rigid grains, as in simulations carried out with the *Contact Dynamics* method [31, 59]. It is indeed widely accepted [2] that elastic deflections in contacts are irrelevant on the scale of the strains (or order 10^{-2} or above) corresponding to the attainment of the peak stress in the dense case or, *a fortiori*, to the approach to the critical state. Yet, at the very beginning of the triaxial test, within the quasielastic range, strains are directly related to contact deflections, resulting from material strain in the intergranular contact regions at small scale. How the initial regime with strains associated with contact deflections is replaced by the strains associated with rearrangements, which no longer depend on contact stiffnesses, is worth investigating [78–81]. The difference between very dense initial states (type A of Sects. 3.1 and 4) with coordination number near 6 under small pressure, on the one hand, and equally dense systems with low coordination (type C) is particularly striking in the pre-peak strain range, and relates to their different sensitivity to dimensionless stiffness number κ. Figure 22 shows that the deviator stress and volumetric strain variations with axial strain in A-type samples, assembled with a large coordination number, strongly depend on stiffness level κ (or on confining stress P for given material elasticity). In the elastic range, strains under given P should vary approximately as $P^{2/3}$, due to the scaling of stiffnesses as $P^{1/3}$. Upon dividing strains by $(P/P_0)^{2/3}$, one should then renormalize the strains so that, if they are on the scale of elastic strains, then the curve coincides with the ones obtained under reference confining pressure P_0. Once carried out in the second plot of Fig. 22 (choosing $P_0 = 100\,\mathrm{kPa}$) this rescaling operation leads to a successful collapse of the different curves onto a single one, in a small initial strain range, within which ratio q/σ_3 raises nearly up to 1. Outside this initial interval (note the fast initial increase of the deviator), the scaling is no longer satisfied.

On the other hand, in C-type systems, as shown in Fig. 23, on the scale of the axial strain corresponding to the deviator peak, the deviator stress and volumetric strain curves do not appear to depend strongly on stiffness level κ-except in some initial range, hardly visible in the main plots Fig. 23, including the elastic range shown in the insets. This regime should correspond to the very fast increase of q

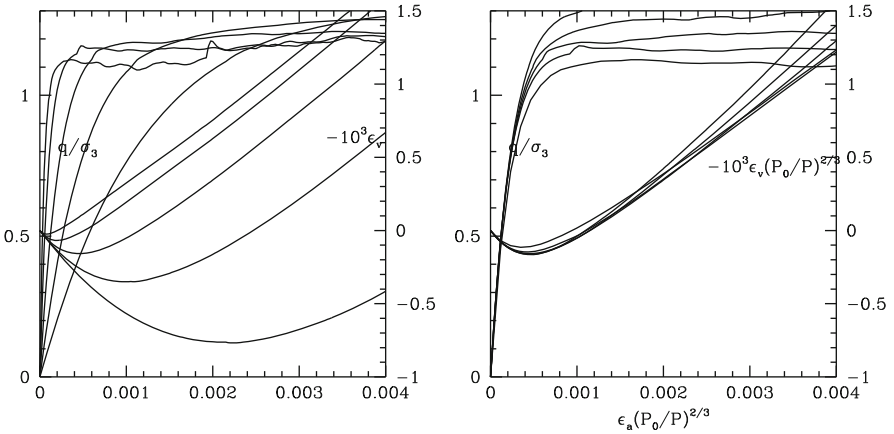

Fig. 22 Normalized deviator q/σ_3 and volumetric strain $-\varepsilon_v$ versus axial strain ε_a in triaxial compression of A-type system with different values of initial isotropic pressure $P = \sigma_3$, from 10 kPa ($\kappa \simeq 39{,}000$) to 1 MPa ($\kappa \simeq 1800$). Left: natural strains; right: rescaled strains, using $P_0 = 100$ kPa

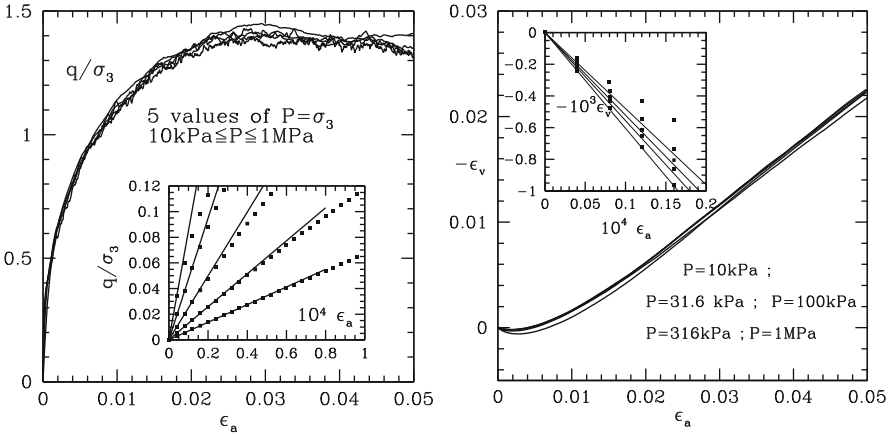

Fig. 23 Normalized deviator q/σ_3 (left) and volumetric strain $-\varepsilon_v$ versus axial strain ε_a (right) in triaxial compression of C-type system with different values of initial isotropic pressure $P = \sigma_3$. Insets show very small strain range, with straight line slopes equal to elastic prediction

(the part of the curve confused with the axis). The very different approach to the peak deviator between A and C systems, with a much faster initial increase in case A (for which the stiffness scales with the elastic stiffness), should be noted. For $\sigma_3 = 100$ kPa, $q/\sigma_3 = 1$ is reached near $\varepsilon_a = 4.10^{-4}$ or A, near 8.10^{-3} for C. However, the value of the peak deviator is near $q = 1.38 \times \sigma_3$ in both systems (see Fig. 9 for A). While the strain curves are strongly different in the first part of the

pre-peak range, both systems A and C, which have the same initial density, exhibit the same peak strength.

In Refs. [48, 80, 81] the strains due to varying contact deflections, characterizing the response of A-type systems (in which the initial coordination number is very high) as shown in Fig. 22, for $q/\sigma_3 \leq 1$, are termed "type I strains". Strains stemming mainly from network breakage and rearrangement, occurring for higher deviators in A samples, and dominating the response of poorly coordinated C samples, as shown in Fig. 23, at least for $q/\sigma_3 \geq 0.2$, are referred to as "type II strains". Type I strains, although their scale is determined by the elasticity of the contact network, are not elastic, because of Coulomb friction. In a type I strain regime, as long as the contact network does not break, a purely static simulation method may be adopted instead of standard dynamical DEM. The contact network is dealt with as a set of connected elastic springs and plastic sliders. Such static methods [48, 78] are based on elastoplastic stiffness matrices, similarly to finite element computations in elastoplastic problems of continuum mechanics, and dispense with all dynamical ingredients of DEM computations, i.e., inertia and viscous forces. Interesting examples and discussions of the applicability of such approaches are to be found in papers by McNamara and coworkers [82–84]. If the initial coordination number can be inferred from the values of elastic moduli, then measurements of the initial, very small strain, quasielastic response could provide useful information—extension of some type I strain regime—on the stress-strain curves in the pre-peak strain interval.

5.3 Irreversibility and Anelasticity: Elastic Range

The irreversibility of the deviator stress variation in triaxial tests is a well-known phenomenon, and its occurrence within the initial regime of type I strains is illustrated in Fig. 24, showing that the unloading branches do not retrace the loading curve back. The deviator stress on unloading will decrease to zero without cancelling the accumulated axial strain, and the residual part of ε_a increases in proportion with the amplitude of the deviator cycle. In Fig. 24, the results of a DEM computation of the triaxial compression test without creation of new contacts are also presented, showing its coincidence with the complete calculation in an initial type I strain regime, observed as long as the initial contact network is able to support the growing deviator stress. Note the different stress and strain scales on the two graphs, highlighting the different behaviours according to coordination number (let us recall that both initial states are isotropic, with the same density). Regime I (i.e., with type I strains) extends to about $\varepsilon_a = 3.10^{-4}$ and $q/\sigma_3 = 0.9$ in case A and to nearly $\varepsilon_a = 10^{-4}$ and $q/\sigma_3 = 0.15$ in case C. It should also be noted that the slope of the unloading curves coincides with the initial elastic modulus, showing that friction mobilization, the physical origin of anelasticity and softening in the forward loading direction, is suppressed in the initial stage of unloading (the change of direction in volumetric strain curves on reversing the loading direction, more

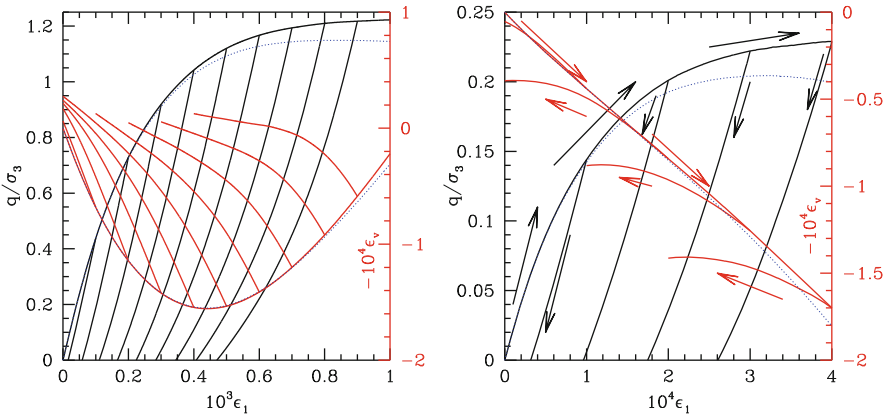

Fig. 24 Behaviour of dense systems upon load reversal (reversing of the sign of $\dot{\varepsilon}_a$) at different stages within initial regime of type I strain in triaxial compression at constant lateral stress 100 kPa. Left: high coordination number (A). Right: low coordination number (C). Thin dotted lines: response on ignoring the creation of new contacts

obviously in the first graph, also tends to return to the initial quasielastic slope). The elastic or quasielastic range was investigated in [38] for the isotropic state at the beginning of such triaxial test, with results analogous to those of Figs. 20 and 19 (corresponding to oedometric compression): elastic ranges are of order 10^{-6} or 10^{-5}, tend to grow like $\sigma_3^{2/3}$, and correspond to relative deviator increases $\Delta q/\sigma_3$ of the order of a few times 10^{-2}.

One may also evaluate elastic properties along the triaxial loading curve, first equilibrating the configuration under constant stresses, thereby causing small creep motion and strain intervals, as shown in Fig. 25. The second graph in Fig. 25 shows that, after equilibrating intermediate states along the triaxial loading curve, the obtained contact networks respond quasielastically to very small stress or strain increments in the forward loading direction, with an initial stiffness, upon resuming the DEM-simulated triaxial compression, equal in good approximation to the one evaluated in static computations using the contact elastic stiffness matrix. The response in unloading (not shown here) exhibits a larger quasielastic interval.

5.4 Some Conclusions and Remarks

The correlations one may find between elastic moduli and internal variables in configurations along the triaxial loading curve prove, as expected, quite similar to the ones observed in oedometric compression (Sect. 4). As the material state evolves towards the critical state, the coordination number quickly evolves (Fig. 10) to a small value ($z^* \sim 4.5 - 4.7$ for $\sigma_3 = 100$ kPa, or $\kappa \simeq 8400$, not too far from the rigid limit). This is similar, for the same range of average pressure, to

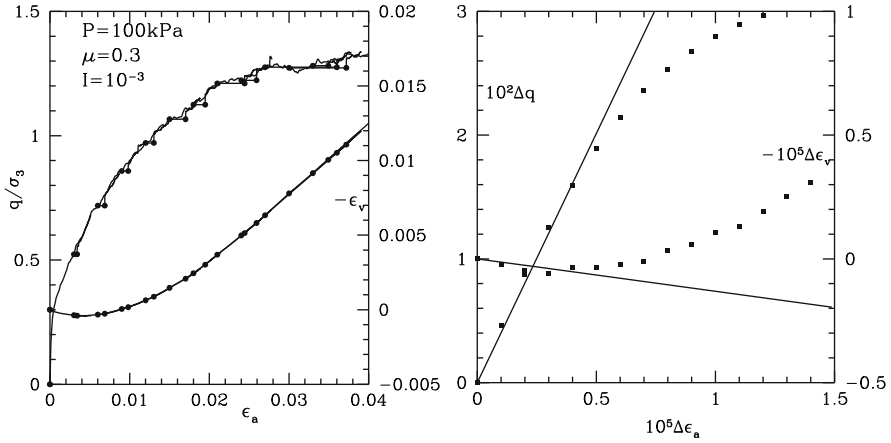

Fig. 25 Left: equilibration after small creep strain interval (beginning and end marked by round dots), followed by resumed strain rate-controlled loading. Right: deviator and volumetric strain curves, on small scale, upon resuming loading from equilibrated configurations. Straight lines: elastic response

z^* values observed in states C, D, L, DL and LL, under isotropic or oedometric compression, initially assembled as poorly coordinated. Elastic moduli exhibit the specific properties observed in isotropic or oedometric loading: anomalously small shear moduli, poor performance of Voigt approximation (see Figs. 12, 13, and 21). Meanwhile, the force network anisotropy increases, reaching levels similar to the ones observed in oedometric compression (see Figs. 3 and 10) whence a similar anisotropy in the tensor of elastic moduli in triaxial as in oedometric compression (see Figs. 16 and 21). The elastic moduli of the states reached along the triaxial loading curve, as anticipated, do not show any sign of the material incipient yield.

One major difference between isotropic or oedometric compressions, up to very large stresses, on the one hand, and triaxial compression, up to large strains and to the critical state, on the other hand, is that the magnitude of strains, in the second case, is such that the material gets strongly restructured. Elastic behaviour could be expected in isotropic or oedometric compression, and the stress-strain relations may seem reversible in such cases (Fig. 5). However, the evolution of internal variables (see Fig. 6 for coordination numbers) and the behaviour of stress ratio K_0 (Fig. 7) clearly show that the response to such compression tests is inherently irreversible and anelastic. On the other hand, one may expect the stress and strain curves in a triaxial compression test to be completely insensitive to contact elasticity, as the behaviour is dominated by the contact network rearrangements. This proves correct for type II strains, but a regime characterized by type I strains, the scale of which is set by the stiffness number κ. Such a regime is present in the beginning of a triaxial compression from isotropically prepared initial packings, and tends to reappear upon unloading, even in rearrangement regimes for which type II strains dominate the material behaviour in forward loading [78].

The existence of a small quasielastic regime in well-equilibrated numerical configuration, once the material sample has acquired a stable contact network and remaining vibrations have been damped out, appears to be a constant feature, occurring even in configurations along the triaxial loading path close to the yield limit. Even though the creep or shakedown stage observed before the quasielastic behaviour is recorded has different causes in simulations and in laboratory experiments, the phenomenon is similar. In this small range (sometimes called “elastic bubble") about a well-stabilized equilibrium state, one observes an elastic response, with a tensor of elastic moduli, endowed with all classical symmetries, expressing the linear dependence of stress increments on strain increments; approximate for finite increments, those stress-strain relations become very nearly exact in the limit of small amplitudes. The slope of stress-strain curves, however, differs, as shown in Fig. 25, before and after creep and full equilibration. Before creep, as the material is being deformed at controlled $\dot{\varepsilon}_a$, due to contact sliding and/or continuous network rearrangements, the stress-strain evolution is considerably softer than the one observed right after equilibrium, upon resuming triaxial loading, when a stabler contact network in which friction is not completely mobilized is being probed. Investigating the full response to incremental stress probes is one way to clarify such issues, as attempted in the 2D studies reported in the next section.

6 Some Investigations of Incremental Elastoplasticity

We report in this section on the investigations [85] of the effect of stress probes incrementally applied to equilibrated granular materials, carried out in two-dimensional (2D) disk samples, along the biaxial test loading trajectory. Similar studies have been carried out by several groups [86, 87], with the objective, in particular, of testing instability criteria based on incremental constitutive laws [75]. The study recalled here [85] was carried out with attention to the influence of initial coordination number (as in the previous sections for 3D simulations), and stiffness level. The biaxial test is similar to the triaxial test of Sect. 3.3, except that there is only one transverse direction (labelled here with index 1) to the axial direction (index 2), which is the major principal stress direction. The typical results of such tests on samples of 5600 polydisperse disks (with a uniform distribution of radii between $R_{\min}$ and $R_{\max} = 13R_{\min}/7$) are shown in Fig. 26. Those biaxial tests are carried out starting with isotropic systems under pressure P, under constant lateral stress $\sigma_1 = P$. The curves of Fig. 26, showing the variations of normalized deviator stress $q/P = (\sigma_2 - \sigma_1)/P$ and “volumetric” strain $\varepsilon_v = 1 - (1 - \varepsilon_1)(1 - \varepsilon_2)$ pertain to a dense, poorly coordinated sample analogous to 3D systems labelled C in the previous sections. Along such curves, *investigation points* are chosen, corresponding to different values of principal stress ratio $\zeta = \sigma_2/\sigma_1$. In those points, after equilibrating the system with good accuracy under the current values of σ_1, σ_2, stress increments of growing amplitudes along different directions in plane σ_1, σ_2 are applied, as indicated in Fig. 27 (16 different directions, 12 values

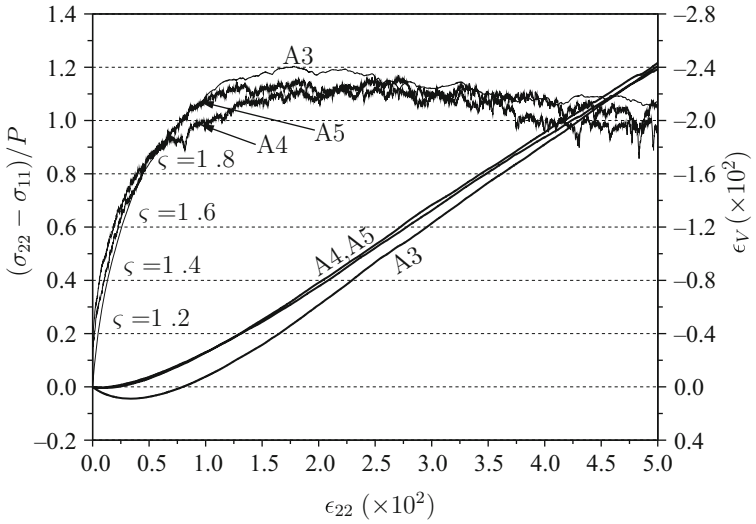

Fig. 26 Biaxial test on dense sample with low coordination number, for different stiffness number κ: 10^5, 10^4 and 10^3. Written values of ς correspond to chosen investigation points

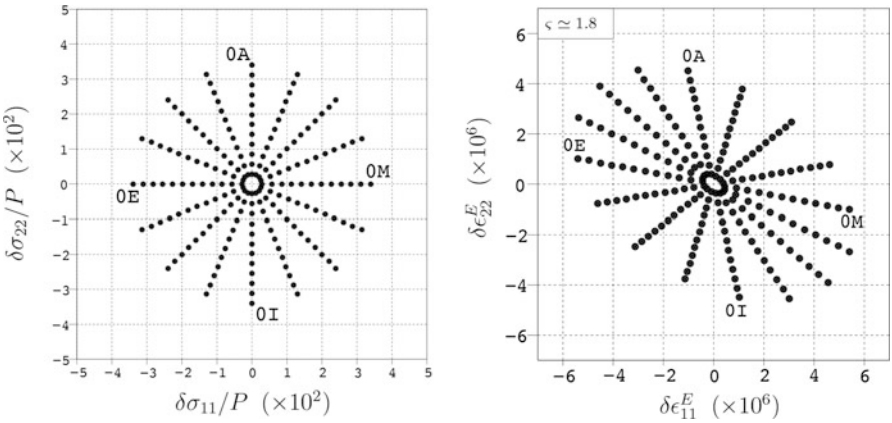

Fig. 27 Applied stress increments (left), example of resulting elastic strain increments (right)

of the amplitude in this case), and the system carefully equilibrated after each new increment. Adopting vector notations for stress and strain (three-dimensional, symmetric tensors in 2D), the aim of such studies is the identification of direction-dependent compliance tensors $\underline{\underline{\mathbf{M}}}$ such that the relation between increments $\delta\boldsymbol{\sigma}$ and $\delta\boldsymbol{\varepsilon}$ takes the form

$$\delta\boldsymbol{\varepsilon} = \underline{\underline{\mathbf{M}}}\left(\frac{\delta\boldsymbol{\sigma}}{||\delta\boldsymbol{\sigma}||}\right)\cdot\delta\boldsymbol{\sigma}. \tag{37}$$

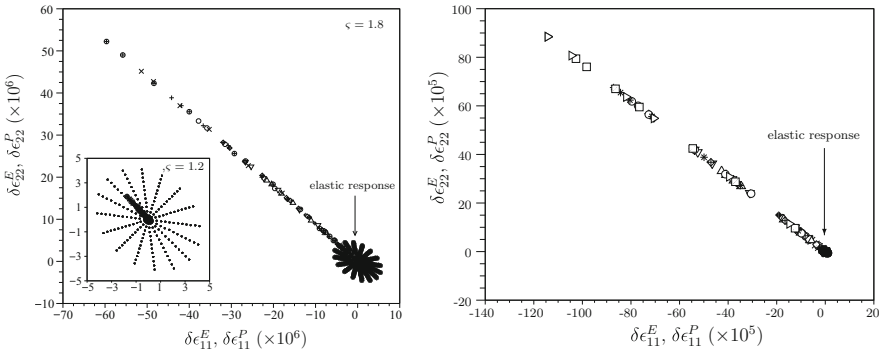

Fig. 28 Decomposition of strain increments into elastic and plastic parts. Left: stress probes in type I strain regime with $\zeta = 1.8$ (main plot) or $\zeta = 1.2$ (inset). Right: stress probes in type II strain regime ($\zeta = 1.8$)

Using the elastic compliance matrix, $\underline{\underline{\mathbf{M}}}^E$, associated with the contact network ($\underline{\underline{\mathbf{M}}}^E$ does not depend on the direction $\frac{\delta\boldsymbol{\sigma}}{||\delta\boldsymbol{\sigma}||}$ of $\delta\boldsymbol{\sigma}$ in stress space) one may extract the elastic part $\delta\boldsymbol{\varepsilon}^E = \underline{\underline{\mathbf{M}}}^E \cdot \delta\boldsymbol{\sigma}$ of the strain increment response. $\delta\boldsymbol{\varepsilon}^E$ is shown in Fig. 27 for one particular investigation point. The elastic compliance tensor $\underline{\underline{\mathbf{M}}}^E$ is computed similarly to the 3D calculations of the previous sections, based on the stiffness matrix of the contact network. The transformation of isotropically oriented $\delta\boldsymbol{\sigma}$ values into an ellipse of $\delta\boldsymbol{\varepsilon}$ values reflects the anisotropy of tensor $\underline{\underline{\mathbf{M}}}^E$. The plastic (or anelastic) part of the strain increment is defined as $\delta\boldsymbol{\varepsilon}^P = \delta\boldsymbol{\varepsilon} - \delta\boldsymbol{\varepsilon}^E$. On subtracting $\delta\boldsymbol{\varepsilon}^E$ from the total strain increment, a plastic component $\delta\boldsymbol{\varepsilon}^P$ is defined, which, as apparent in Fig. 28, stays in a well-defined *flow direction* for all stress increments $\delta\boldsymbol{\sigma}$ within the σ_1, σ_2 plane. According to the probed investigation point, the relative importance of elastic and plastic strains varies considerably. The total strain increment for a given deviator increase should become larger and larger as the deviator curve softens. Consequently, as the elastic moduli remain of the same order and the elastic strain does not increase, the strain gradually becomes mostly plastic. In the case of type II strains (right graph in Fig. 28), the scale of global strains is set by network rearrangements and the elastic term $\delta\boldsymbol{\varepsilon}^E$ becomes negligible.

An incremental law in the form of Eq. (37) should also imply the identification of a plastic criterion, and of a plastic modulus E^P, such that the magnitude of the plastic strain increment is proportional to the stress increment projected along the outward normal $\boldsymbol{\xi}$ in stress space. The choice of $\boldsymbol{\xi}$ is the one leading to a linear relation between $[\boldsymbol{\xi} \cdot \delta\boldsymbol{\sigma}]_+$ (the positive part of $\boldsymbol{\xi} \cdot \delta\boldsymbol{\sigma}$, equal to itself if positive, to zero otherwise) and $||\delta\boldsymbol{\varepsilon}^P||$,

$$||\delta\boldsymbol{\varepsilon}^P|| = \frac{1}{E^P} [\boldsymbol{\xi} \cdot \delta\boldsymbol{\sigma}]_+ , \tag{38}$$

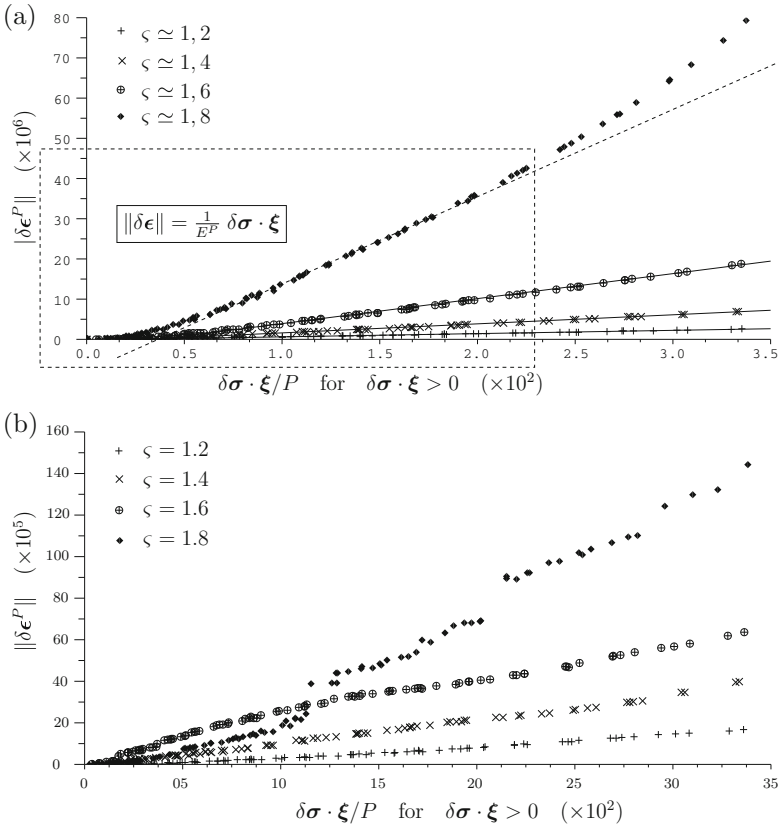

Fig. 29 $||\delta\boldsymbol{\epsilon}^P||$ versus $[\boldsymbol{\xi}\cdot\delta\boldsymbol{\sigma}]_+$, for different stress ratios ζ and $\kappa = 10^4$. (**a**): type I strains. (**b**): type II strains

as represented in Fig. 29. In good approximation, it is observed that direction $\boldsymbol{\xi}$ is orthogonal to the vector of coordinates σ_1, σ_2 in stress space, oriented in the direction of growing principal stress ratio σ_2/σ_1. The directional linearity (or positive homogeneity of order (1) expressed by Eqs. (37) and (38) is obtained in practice with an appropriate choice of increment sizes. With too large increments the linearity is lost as the stress-strain curve departs from its tangent. With very small increments, greater computational accuracy could be required. Note also that one may observe the "elastic bubble" phenomenon mentioned in Sect. 5.4: a small interval $[\boldsymbol{\xi}\cdot\delta\boldsymbol{\sigma}]_+^E$ of $[\boldsymbol{\xi}\cdot\delta\boldsymbol{\sigma}]_+$ entails no plastic strain. This is apparent, in particular, in the data of Fig. 29a pertaining to stress ratio $\zeta = 1.8$. Thus the linear law written in (38) applies to some difference $[\boldsymbol{\xi}\cdot\delta\boldsymbol{\sigma}]_+ - [\boldsymbol{\xi}\cdot\delta\boldsymbol{\sigma}]_+^E$.

In the case of strains of type II, caused by instabilities and rearrangements of the network, the hardening modulus has to be identified from the slope of a staircase-shaped curve, as shown in Fig. 29b, corresponding to the discontinuous appearance of the second plot of Fig. 28.

These results should be generalized to three-dimensional stress space in 2D, before dealing with 3D systems. Preliminary results show then that the applications of increments of shear stress σ_{12} always cause plastic strains, and that the incremental law (37) relates stress and strain increments both spanning a two-dimensional space [85].

7 A Few Remarks and Perspectives

As announced, and commented in Sect. 5.4, the measurement of elastic moduli, although indicative of some properties of the contact network (coordination number, fabric, and, to a lesser extent, anisotropy of forces), does not provide information about incipient failure modes. This information, on the other hand, is contained in the incremental anelastic response, which may apparently be described, to some extent, with the ingredients of elastoplastic models: flow rule, criterion, plastic hardening modulus (although some results, not reported in Sect. 6, imply that several plasticity mechanisms are required). Singularities in the elastic response occur in poorly connected contact networks with very small force indeterminacy. Systems with vanishing degree of force indeterminacy are observed with frictionless grains, but are not usually obtained in the presence of friction. The absence of observed elastic singularity in assemblies of frictional grains is related to the conditions for observing elastic properties, which usually imply a stable network and negligible effects of friction forces in contacts. The exploration of the incremental behaviour of granular materials outside a quasielastic range is difficult. Experimentally, it is impossible to repeat the test with the same sample as the material state is bound to evolve irreversibly. One thus needs to prepare, e.g., as many samples in the same state as there are directions of stress increments to probe, a cumbersome and technically challenging task. Numerically, although it is feasible to apply different probes to the same system, one has to characterize a behaviour from the noisy response of systems of relatively small size, especially on dealing with strains “of type II", caused by network failure and rearrangements. Careful and statistically representative tests still need to be carried out to understand frictional failure of contact networks, and how such accumulated events, in which the networks get repeatedly broken and repaired, give rise to well-defined stress-strain relations, involving fabric and friction mobilization evolutions.

References

1. B. Andreotti, Y. Forterre, and O. Pouliquen. *Granular Media: Between Fluid and Solid*. Cambridge University Press, Cambridge, UK, 2013.
2. J.-N. Roux and F. Chevoir. Dimensional Analysis and Control Parameters. In Radjaï and Dubois [88], chapter 8, pages 199–232.

3. P. Vermeer. A five constant model unifying well established concepts. In *International Workshop on Constitutive Behaviour of Soils*, pages 175–197, Grenoble, 1982. Balkema.
4. D. M. Wood. *Soil Behaviour and Critical State Soil Mechanics*. Cambridge University Press, 1990.
5. P. A. Vermeer. Non-associated plasticity for soils, concrete and rock. In H. J. Herrmann, J.-P. Hovi, and S. Luding, editors, *Physics of Dry Granular Media*, pages 163–196, Dordrecht, 1998. Balkema.
6. J.K. Mitchell and K. Soga. *Fundamentals of Soil Behavior*. Wiley, 2005.
7. S Shibuya, F. Tatsuoka, S. Teachavorasinskun, X.-J. Kong, F. Abe, Y.-S. Kim, and C.-S. Park. Elastic deformation properties of geomaterials. *Soils and Foundations*, 32:26–46, 1992.
8. P.-Y. Hicher. Elastic properties of soils. *ASCE Journal of Geotechnical Engineering*, 122:641–648, 1996.
9. R. Kuwano and R. J. Jardine. On the applicability of cross-anisotropic elasticity to granular materials at very small strains. *Géotechnique*, 52:727–749, 2002.
10. H. Geoffroy, H. di Benedetto, A. Duttine, and C. Sauzéat. Dynamic and cyclic loadings on sands: results and modelling for general stress-strain conditions. In di Benedetto et al. [89], pages 353–363.
11. A. Ezaoui and H. di Benedetto. Experimental measurements of the global anisotropic elastic behaviour of dry Hostun sand during triaxial tests, and effect of sample preparation. *Géotechnique*, 59(7):621–635, 2009.
12. Y.-C. Chen, I. Ishibashi, and J. T. Jenkins. Dynamic shear modulus and fabric: part i, depositional and induced anisotropy. *Géotechnique*, 38(1):23–32, 1988.
13. Y.-C. Chen, I. Ishibashi, and J. T. Jenkins. Dynamic shear modulus and fabric: part ii, stress reversal. *Géotechnique*, 38(1):33–37, 1988.
14. Thomas G. Thomann and Roman D. Hryciw. Laboratory measurement of small strain shear modulus under K_0 conditions. *ASTM Geotechnical Testing Journal*, 13(2):97–105, 1990.
15. X. Jia, C. Caroli, and B. Velický. Ultrasound propagation in externally stressed granular media. *Phys. Rev. Lett.*, 82:1863–1866, 1999.
16. X. Jia and P. Mills. Sound propagation in dense granular materials. In Y. Kishino, editor, *Powders and Grains 2001*, pages 105–112, Lisse, 2001. Swets & Zeitlinger.
17. I. Agnolin, J.-N. Roux, P. Maassad, X. Jia, and P. Mills. Sound wave velocities in dry and lubricated granular packings: numerical simulations and experiments. In R. García Rojo, H. J. Herrmann, and S. McNamara, editors, *Powders and Grains 2005*, pages 313–317, Leiden, 2005. Balkema.
18. Y. Khidas and X. Jia. Anisotropic nonlinear elasticity in a spherical bead pack: influence of the fabric anisotropy. *Phys. Rev. E*, 81:021303, 2010.
19. H. A. Makse, N. Gland, D. L. Johnson, and L. Schwartz. Granular packings: Nonlinear elasticity, sound propagation, and collective relaxation dynamics. *Phys. Rev. E*, 70:061302, 2004.
20. N. P. Kruyt. Micromechanical study of elastic moduli of three-dimensional granular assemblies. *International Journal of Solids and Structures*, 51:2336–2344, 2014.
21. A. S. J. Suiker and N. A. Fleck. Frictional collapse of granular assemblies. *ASME Journal of Applied Mechanics*, 71:350–358, 2004.
22. C. O'Hern, L. E. Silbert, A. J. Liu, and S. R. Nagel. Jamming at zero temperature and zero applied stress: The epitome of disorder. *Phys. Rev. E*, 68(1):011306, 2003.
23. H. P. Zhang and H. A. Makse. Jamming transition in emulsions and granular materials. *Phys. Rev. E*, 72:011301, 2005.
24. M. Wyart. On the rigidity of amorphous solids. *Annales de Physique Fr.*, 30:1–96, 2006.
25. Ellák Somfai, Martin van Hecke, Wouter G. Ellenbroek, Kostya Shundyak, and Wim van Saarloos. Critical and noncritical jamming of frictional grains. *Phys. Rev. E*, 75(2):020301, 2007.
26. L. La Ragione and V. Magnanimo. Contact anisotropy and coordination number for a granular assembly: A comparison of distinct-element-method simulations and theory. *Phys. Rev. E*, page 031304, 2012.

27. L. La Ragione and V. Magnanimo. Evolution of the effective moduli of an anisotropic, dense, granular material. *Granular Matter*, 14:749–757, 2012.
28. M. H. Khalili, J.-N. Roux, J.-M. Pereira, S. Brisard, and M. Bornert. Numerical simulation of one-dimensional compression of granular materials: II. Elastic moduli, stresses and microstructure. *Phys. Rev. E*, 95:032908, 2017.
29. F. Radjaï, H. Troadec, and S. Roux. Basic features of granular plasticity. In S. J. Antony, W. Hoyle, and Y. Ding, editors, *Granular Materials: Fundamentals and Applications*, pages 157–183, Cambridge, 2004. Royal Society of Chemistry.
30. F. Radjaï, J.-Y. Delenne, E. Azéma, and S. Roux. Fabric evolution and accessible geometrical states in granular materials. *Granular Matter*, 14:259–264, 2012.
31. E. Azéma, F. Radjaï, and F. Dubois. Packings of irregular polyhedral particles: Strength, structure, and effects of angularity. *Phys. Rev. E*, 87:062223, 2013.
32. M. Jean. The non-smooth contact dynamics method. *Computational Methods in Applied Engineering*, pages 235–257, 1999.
33. F. Radjaï and V. Richefeu. Contact dynamics as a nonsmooth discrete element method. *Mechanics of Materials*, 41:715–728, 2009.
34. Y. Jiang and M. Liu. Granular solid hydrodynamics. *Granular Matter*, 11:139–156, 2009.
35. YM Jiang and M. Liu. Granular Solid Hydrodynamics (GSH): a broad-ranged macroscopic theory of granular media. *Acta Mechanica*, 225:2363–2384, 2014.
36. I. Agnolin and J.-N Roux. Internal states of model isotropic granular packings. I. Assembling process, geometry, and contact networks. *Phys. Rev. E*, 76(6):061302, 2007.
37. I. Agnolin and J.-N Roux. Internal states of model isotropic granular packings. II. Compression and pressure cycles. *Phys. Rev. E*, 76(6):061303, 2007.
38. I. Agnolin and J.-N. Roux. Internal states of model isotropic granular packings. III. Elastic properties. *Phys. Rev. E*, 76(6):061304, 2007.
39. J.-N. Roux. DEM simulations of triaxial tests on dense bead assemblies. Unpublished.
40. C. Dequeker and J.-N. Roux. DEM simulations of triaxial tests of loose bead assemblies. Unpublished results.
41. P.-E. Peyneau and J.-N. Roux. Solidlike behavior and anisotropy in rigid frictionless bead assemblies. *Phys. Rev. E*, 78:041307, 2008.
42. M. H. Khalili, J.-N. Roux, J.-M. Pereira, S. Brisard, and M. Bornert. A numerical study of one-dimensional compression of granular materials: I. Stress-strain behavior, microstructure and irreversibility. *Phys. Rev. E*, 95(032907), 2017.
43. K. L. Johnson. *Contact Mechanics*. Cambridge University Press, 1985.
44. D. Elata and J. G. Berryman. Contact force-displacement laws and the mechanical behavior of random packs of identical spheres. *Mechanics of Materials*, 24:229–240, 1996.
45. M. R. Kuhn and C. S. Chang. Stability, Bifurcation and Softening in Discrete Systems: A Conceptual Approach for Granular Materials. *International Journal of Solids and Structures*, 43:6026–6051, 2006.
46. P.-E. Peyneau and J.-N. Roux. Frictionless bead packs have macroscopic friction, but no dilatancy. *Phys. Rev. E*, 78:011307, 2008.
47. F. Radjaï and C. Voivret. Periodic Boundary Conditions. In Radjaï and Dubois [88], chapter 7, pages 181–198.
48. J.-N. Roux and G. Combe. Quasi-Static Methods. In Radjaï and Dubois [88], chapter 3, pages 67–101.
49. V.-D. Than, S. Khamseh, A. M. Tang, J.-M. Pereira, F. Chevoir, and J.-N. Roux. Basic Mechanical Properties of Wet Granular Materials: A DEM Study. *ASCE Journal of Engineering Mechanics*, 2016.
50. D. M. Mueth, H. M. Jaeger, and S. R. Nagel. Force distribution in a granular medium. *Phys. Rev. E*, 57:3164–3169, 1998.
51. F. Radjaï, S. Roux, and J.-J Moreau. Contact forces in a granular packing. *Chaos*, 9(3):544–550, 1999.

52. D. L. Blair, N. W. Mueggenburg, A. H. Marshall, H.M. Jaeger, and S. R. Nagel. Force distribution in three-dimensional granular assemblies: Effects of packing order and interparticle friction. *Phys. Rev. E*, 63:041304, 2001.
53. F. Radjai. Modeling force transmission in granular materials. *Comptes Rendus Physique*, 16(1):3–9, 2015.
54. H. A. Makse, D. L. Johnson, and L. M. Schwartz. Packing of compressible granular materials. *Phys. Rev. Lett.*, 84(18):4160–4163, 2000.
55. Y. Okuchi and F. Tatsuoka. Some factors affecting K_0 values of sand measured in triaxial cell. *Soils and Foundations*, 24(3):52–68, 1984.
56. Junhwan Lee, Sup Yun Tae, Dongyeol Lee, and Junghwoon Lee. Assessment of K_0 correlation to strength for granular materials. *Soils and Foundations*, 53(4):584–595, 2013.
57. L. Rothenburg and R.J. Bathurst. Analytical study of induced anisotropy in idealized granular materials. *Géotechnique*, 39:601–614, 1989.
58. C. Thornton. Numerical simulations of deviatoric shear deformation of granular media. *Géotechnique*, 50:43–53, 2000.
59. F. Radjaï and S. Roux. Contact dynamics study of 2d granular media : critical states and relevant internal variables. In H. Hinrichsen and D. E. Wolf, editors, *The Physics of Granular Media*, pages 165–187, Berlin, 2004. Wiley-VCH.
60. L. Rothenburg and N. P. Kruyt. Critical state and evolution of coordination number in simulated granular materials. *International Journal of Solids and Structures*, 41(2):5763–5774, 2004.
61. N. P. Kruyt and L. Rothenburg. Shear strength, dilatancy, energy and dissipation in quasistatic deformation of granular materials. *Journal of Statistical Mechanics: Theory and Experiment*, page P07021, 2006.
62. C. Thornton and L. Zhang. On the evolution of stress and microstructure during general 3D deviatoric straining of granular media. *Géotechnique*, 60(5):333–341, 2010.
63. J. T. Jenkins and L. La Ragione. Particle spin in anisotropic granular materials. *International Journal of Solids and Structures*, 38:1063–1069, 2001.
64. C. Gay and R. A. da Silveira. Anisotropic elastic theory of preloaded granular media. *Europhysics Letters*, 68:51–57, 2004.
65. L. La Ragione and J. T. Jenkins. The initial response of an idealized granular material. *Proceedings of the Royal Society A*, 63(2079):735–758, 2007.
66. I. Agnolin and J.-N. Roux. On the elastic moduli of three-dimensional assemblies of spheres: Characterization and modeling of fluctuations in the particle displacement and rotation. *International Journal of Solids and Structures*, 45(3–4):1101–1123, 2008.
67. E. Somfai, J.-N. Roux, J. H. Snoeijer, M. van Hecke, and W. van Saarloos. Elastic wave propagation in confined granular systems. *Phys. Rev. E*, 72:021301, 2005.
68. J.-N. Roux. Geometric origin of mechanical properties of granular materials. *Phys. Rev. E*, 61:6802–6836, 2000.
69. L. E. Silbert, D. Ertaş, G. S. Grest, T. C. Halsey, and D. Levine. Geometry of frictionless and frictional sphere packings. *Phys. Rev. E*, 65(3):031304, 2002.
70. A. Donev, S. Torquato, and F. H. Stillinger. Pair correlation function characteristics of nearly jammed disordered and ordered hard-sphere solids. *Phys. Rev. E*, 71(1):011105, 2005.
71. M. Baity-Jesi, C.P. Goodrich, A.J. Liu, and J.P. Nagel, S. R. Sethna. Emergent SO(3) Symmetry of the Frictionless Shear Jamming Transition. *Journal of Statistical Physics*, 167:735–748, 2017.
72. A. Duttine, H. Di Benedetto, D. Pham Van Bang, and A. Ezaoui. Anisotropic small strain elastic properties of sands and mixture of sand-clay measured by dynamic and static methods. *Soils and Foundations*, 47(3):457–472, 2007.
73. E. T. Bowman and K. Soga. Creep, ageing and microstructural change in dense granular materials. *Soils and Foundations*, 43:107–117, 2003.
74. Y. Gao, Y.-H. Wang, and J.C.P. Xu. Mechanisms of Aging-Induced Modulus Changes in Sand under Isotropic and Anisotropic Loading. *ASCE J. Geotech. Geoenviron. Eng*, 139:470–482, 2013.

75. I. Vardoulakis and J. Sulem. *Bifurcation Analysis in Geomechanics*. Blackie Academic and Professional, 1995.
76. J. Desrues, R. Chambon, M. Mokni, and F. Mazerolle. Void ratio evolution inside shear bands in triaxial sand specimens studied by computed tomography. *Géotechnique*, 46:529–546, 1996.
77. S. Fazekas, J. Török, and J. Kertész. Critical packing in granular shear bands. *Phys. Rev. E*, 2007.
78. J.-N. Roux and G. Combe. Quasistatic rheology and the origins of strain. *C. R. Physique*, 3:131–140, 2002.
79. G. Combe and J.-N. Roux. Discrete numerical simulations, quasistatic deformation and the origins of strain in granular materials. In di Benedetto et al. [89], pages 1071–1078.
80. J.-N. Roux and G. Combe. How granular materials deform in quasistatic conditions. In Goddard et al. [90], pages 260–270.
81. J.-N. Roux. Pre-peak deformation of model granular materials: A DEM study. In K. Soga, K. Kumar, G. Biscontin, and M. Kuo, editors, *Geomechanics from micro to macro*, pages 49–54. CRC-Press-Taylor & Francis, 2015.
82. S. McNamara, R. García Rojo, and H. J. Herrmann. Indeterminacy and the onset of motion in a simple granular packing. *Phys. Rev. E*, 72:021304, 2005.
83. S. McNamara and H. J. Herrmann. Quasirigidity: some uniqueness issues. *Phys. Rev. E*, 74:061303, 2006.
84. P. R. Welker and S. C. McNamara. What triggers failure in frictional granular assemblies? *Phys. Rev. E*, 79:061305, 2009.
85. F. Froiio and J.-N. Roux. Incremental response of a model granular material by stress probing with DEM simulations. In Goddard et al. [90], pages 260–270.
86. F. Alonso-Marroquin and H. J. Herrmann. Calculation of the incremental stress-strain relation of a polygonal packing. *Phys. Rev. E (2002) 66:021301*, 66:021301, 2005.
87. C Tamagnini, F. Calvetti, and G. Viggiani. An assessment of plasticity theories for modelling the incrementally non-linear behavior of granular soils. *ASCE Journal of Engineering Mechanics*, 52:265–291, 2005.
88. F. Radjaï and F. Dubois, editors. *Discrete-element modeling of granular materials*. Wiley, 2011.
89. H. di Benedetto, T. Doanh, H. Geoffroy, and C. Sauzéat, editors. *Deformation characteristics of geomaterials*, Lisse, 2003. Swets and Zeitlinger.
90. J. D. Goddard, J. T. Jenkins, and P. Giovine, editors. *IUTAM-ISIMM symposium on mathematical modeling and physical instances of granular flow*, volume 1227 of *AIP conference proceedings*. AIP, 2010.